Large Eddy Simulation of A Three-DimensionalCompression Ramp Shock-Turbulent Boundary Layer Interaction

D. Dawson, S. K. Lele

November 24, 2014

AIAA Aerospace Sciences Meeting
Kissimmee, FL, United States
January 5, 2015 through January 9, 2015

Disclaimer

Large Eddy Simulation of A Three-Dimensional Compression Ramp Shock-Turbulent Boundary Layer Interaction

David M. Dawson*
Stanford University, Stanford, CA 94305, USA
and Lawrence Livermore National Laboratory, Livermore, CA 94550, USA,
and Sanjiva K. Lele†
Stanford University, Stanford, CA 94305, USA

Large-Eddy Simulation (LES) is used to investigate the flow physics of a Three-Dimensional Shock-Turbulent Boundary Layer Interaction (3D-STBLI). We consider a supersonic turbulent boundary layer with a free stream Mach number of $M_\infty = 2.9$ and Momentum Thickness Reynolds number of $Re_\theta = 2400$ as it flows over a 24° compression ramp with flow confining aerodynamic fences (AF). Results are compared against the experimental data of Ringuette *et al.*, 2009, at matching conditions and geometry. In the region near the aerodynamic fences, the shock system and separation bubble are significantly distorted away from the nominally two dimensional structure. The assumption in most experimental and numerical investigations is that the flow conditions in the middle of the ramp are sufficiently unaffected by these distortions and regains a two-dimensional span-periodic behavior. Additionally the assumption is usually made that the flow is statistically homogeneous in the spanwise direction. This investigation seeks to quantify the validity of these assumptions as well as to investigate the complex flow phenomena present near the aerodynamic fences. Validation of the numerical results against experimental data is presented as well as a comparison against a span-periodic calculation. A detailed investigation into the span-wise variation of several important quantities, such as separation length, skin friction coefficient, and properties of low-frequency dynamics, is performed and discussed. Görtler-like vortices are found to cause significant spanwise inhomogeneities in the flow.

Nomenclature

x, y, z	Cartesian Coordinates	μ	Molecular viscosity
ξ, η	Ramp Aligned Coordinates	c	Sound speed
s	Distance along a streamline	β	Ramp angle
t	Time	M	Mach number
τ	Non-dimensional time	Re	Reynolds number
f	Frequency	G_T	Görtler number
ρ	Density	Pr_t	Turbulent Prandtl number
u, v, w	Velocity components	St	Strouhal number
E	Total energy	St_{BL}	Boundary layer frequency
p	Pressure	St_{conv}	Convective frequency
T	Temperature	St_{LDT}	Lagrangian decorrelation frequency
T_r	Adiabatic recovery temperature	St_{ET}	Eddy turnover frequency

---

[*] PhD. Candidate, Department of Aeronautics & Astronautics, Stanford University, Stanford, CA 94305, and Computational Physicist, Turbulence Analysis & Simulation Center, Lawrence Livermore National Laboratory, Livermore, CA 94550, AIAA Student Member.

[†] Professor, Department of Aeronautics & Astronautics and Department of Mechanical Engineering, Stanford University, Stanford, CA 94305, AIAA Associate Fellow

δ	Boundary layer thickness
δ^*	Displacement thickness
θ	Momentum thickness
H	Shape factor
C_f	Skin friction coefficient
u_τ	Friction velocity
τ_w	Skin friction
$u_V D^+$	van Driest velocity
Q	Second invarient of velocity gradient
R	Radius of flow curvature
κ	Flow curvature
L_{sep}	Separation length
x_{sep}	Separation point
x_{reat}	Reattachment point
L_z	Spanwise wavelength
κ_z	Spanwise wavenumber
ω_x, ω_y, ω_z	Vorticity components
$E(\,)$	Energy spectral density
$P(\,)$	Power spectral density
$\bigtriangledown$	Gradient operator
κ^*, C	van Driest constants
Subscript	
w	Wall quantity
∞	Free stream quantity
Superscript	
$+$	Wall unit quantity
$\overline{}$	Time averaged quantity
$'$	Fluctuation quantity

I. Introduction

Shock-turbulent boundary layer interaction (STBLI) can have a dramatic impact on the unsteady aerodynamic and thermal loads on supersonic and hypersonic vehicle components. STBLI associated with inlets and the inlet/isolator of supersonic combustion ramjet (SCRAMJET) engines can be a performance limiting feature due to the potential for triggering engine unstart[1] as well as the increased heat transfer that can accompany STBLI. Additionally, ineffective control of STBLI can result in a decrease or complete loss of hypersonic vehicle control surface effectiveness.[2] Despite the importance of STBLI in propulsion and aerodynamic systems and more than 60 years of research, we still lack a good understanding of the fundamental physics involved in many aspects of STBLI especially in the complex three-dimensional geometries used in real flight vehicles.

Most numerical investigations of STBLI have utilized Reynolds-averaged Navier-Stokes (RANS) models. However, these have been shown to give poor agreement with experiment.[3,4] The poor performance of RANS models in simulating STBLI can at least partially be attributed to the low-frequency unsteadiness often observed in STBLI. These flows exhibit low-frequency motion of both the shock and separation bubble with time scales on the order of $10-100$ times longer than the characteristic time scale of the incoming boundary layer $\tau = \delta/u_\infty$.[2,5–14] Such unsteadiness and its effects are difficult, if not impossible, to capture using the solution of RANS equations because of the time-averaging and equilibrium turbulence assumptions inherent in RANS. Errors in the RANS models themselves can also lead to widely different solutions of STBLI flows depending on the model chosen and the settings used, leading to a considerable amount of epistemic uncertainty in the calculations. Morgen *et al.* observed consistent overprediction of seperation length of up to 100% in their investigation of an Oblique Shock-Turbulent Boundary Layer Interaction using several RANS models.[15,16]

High-fidelity numerical techniques, such as DNS and LES, are enabling more accurate study of STBLI and the unsteady phenomena with which it is associated.[2,10,13–15,17–29] However, when applied to turbulent boundary layers and STBLI at high Reynolds numbers, the computational cost of these approaches becomes highly prohibitive. Wall bounded turbulence is a multi-scale phenomena in which the energetic motions of the inner layer (closest to the wall) become progressively smaller in size as the Reynolds number increases. However, the experimental work by Ringuette *et al.*[30] and related work,[31] has been conducted at LES/DNS accessible Reynolds numbers and has proved valuable as a means of validation of high-fidelity calculations of this configuration.[2,18,19,32] Numerical studies of this configuration to date, have all made the assumption of span-wise periodicity, whereas in real world flight vehicles, the STBLI phenomena will always be accompanied by some three-dimensional effects, most often from bounding side-walls. In the case of this study, the nominally two dimensional flow is accompanied by aerodynamic fences to confine the flow over the ramp. The numerical investigation of Hadjadj *et al.*[23,24] included a brief investigation into the effects of slip side walls on an Oblique Shock Reflection STBLI and found that the inclusion of slip side walls formed sidewall vortices, strengthened the interaction, and increased the low-frequency energy content over the spanwise periodic case. A more detailed numerical study performed by Bermejo-Moreno *et al.*[33,34] in conjunction with the experimental work of Helmer *et al.*[35,36] greatly expanded our understanding of the effects of wind tunnel side walls on STBLI for a sub-boundary layer scale full-span compression ramp. They found that the interaction length decreased near the sidewalls and that counter-rotating corner vortices were highly distorted by the interaction, eventually forming a single elongated vorticle structure along the sidewall. This study seeks to expand on these works in the context of a compression ramp STBLI with flow confining aerodynamic fences. This configuration is of great importance to design engineers as aerodynamic fences are often used to control the flow to and near control surfaces to increase their effectiveness as well as in experimental investigations to confine the flow over a body. At hypersonic speeds the large thermal and pressure loads on aerodynamic fences, such as those due to STBLI, may become a critical factor in their design. The objective of this study is to investigate the effects that aerodynamic fences have on a compression ramp STBLI incluidng low-frequency unsteadiness, explore the spanwise periodic, spanwise homogeneous, and narrow spanwise domain assumptions traditionally used in high fidelity numerical investigations of STBLI, and establish LES as a tool suitable for more complex geometries.

We begin by reviewing the numerical approach, geometry, grid, and boundary conditions in Section II. Validation is performed against experimental data at matching conditions in Section III. Section IV presents the results and discussion of three-dimensional aspects of the flow. Section V presents conclusions drawn from this work.

II. Numerical Approach and Problem Setup

A. Numerical Method

In this study we utilize the unstructured LES solver $CharLES^x$, developed at Stanford University's Center for Turbulence Research. We solve the spatially-filtered compressible Navier-Stokes equations in a finite volume form. The conservative variables ρ, ρu, ρv, ρw, and ρE, are solved for, in which ρ is the density, u, v, w are the stream-wise, wall-normal, and span-wise velocities, and E is the total energy. $CharLES^x$ computes the Euler flux using a mix of non-dissipative central flux and dissipative upwind flux. The blend of these two techniques varies spatially based on grid quality. In regions where the grid quality is good and the central flux scheme is linearly stable, the dissipative flux contribution is turned off. In regions of sub-optimal grid quality, the central flux scheme can introduce numerical instabilities that must be prevented by contributions from the dissipative flux. By utilizing a blend of each flux type, the goal is to achieve a numerical method which is as non-dissipative as is achievable on a given mesh. Since the weighting between these two techniques is purely grid based, it can be computed once at the beginning of a calculation. The solution is advanced in time using an explicit $3rd-Order$ Runge-Kutta method. For a more detailed description of the numerical method employed, the reader is referred to Khalighi *et al.*[37]

B. Shock Capturing

$CharLES^x$ utilizes a hybrid Central-ENO scheme to compute flows involving shocks. The method switches between the central scheme described previously and a $2nd$-order ENO method based on a switching function which detects the presence of a shock. In all results presented here, a sensor based on the local dilatation and enstrophy is used to detect the presence of shocks, thus preserving turbulent fluctuations elsewhere in the flow.

C. Sub-grid scale modeling

The numerical method used in $CharLES^x$ has minimal numerical dissipation, therefore it is necessary that a sub-grid model be used to account for the physical effects of unresolved turbulence. In all calculations discussed here, we have utilized the Vreman sub-grid model.[38,39] For the Vreman model, the recommended constant coefficient value of $c = 0.07$ is used, and a turbulent Prandtl number of $Pr_t = 0.9$ is used to close the energy equation.

D. Inflow Turbulence Generation

To avoid the costly procedure of simulating the incoming boundary layer through transition we utilize the synthetic inflow turbulence generation method of Xie & Castro,[40] with the modifications of Touber & Sandham.[28] The method, based on the digital filtering technique of Klein *et al.*[41] is designed to impose specified turbulence mean profiles as well as single- and two-point correlations. The method implemented in $CharLES^x$ has been shown effective for STBLI in previous calculations by Bermejo-Moreno *et al.*[33] and Dawson *et al.*[19] For the calculations presented here, the required turbulence quantities were calculated from a the solution of a previous LES study by Dawson *et al.*[19] of a STBLI at the same conditions.

E. Geometry and Conditions

We match the flow conditions of the experimental investigation of Ringuette et al.[30] and Bookey[31] consisting of a free stream Mach number of $M_\infty = 2.9$, momentum thickness Reynolds number of $Re_\theta = 2400$, and an isothermal wall condition of $T_w/T_\infty = 2.84$ which is $T_w/T_r = 0.95$ where T_r is the adiabatic recovery temperature. Table 1 summarizes the flow conditions of the present study as well as that of the comparison experiment[30] and the DNS study of Wu and Martin.[2,13]

	M_∞	Re_θ	$\delta(mm)$	$\delta^*(mm)$	$\theta(mm)$	H	$C_f \times 10^3$	$u_\tau(m/s)$
Present - LES	2.9	2400	6.7	2.85	0.50	5.7	2.03	32.4
Ringuette *et al.* - Experiment[30]	2.9	2400	6.7	2.36	0.43	5.49	2.17	32.9
Wu & Martin - DNS[2,13]	2.9	2300	6.4	1.80	0.38	4.74	2.17	34.0

Table 1: Flow Conditions. $Re_\theta = \frac{\rho_\infty u_\infty \theta}{\mu_\infty}$, $H = \frac{\delta^*}{\theta}$, $C_f = \frac{\tau_w}{\frac{1}{2}\rho_\infty u_\infty^2}$, $u_\tau = \sqrt{\frac{\tau_w}{\rho_w}}$, and $\tau_w = \mu_w \left|\frac{\partial u}{\partial y}\right|_w$.

The domain consists of a flat plat leading to a $\beta = 24°$ compression ramp with aerodynamic fences on either side. Outside of the aerodynamic fences, the flat plate continues unobstructed. Our reference length, δ, is chosen as the boundary layer thickness $60mm$ (9δ) upstream of the corner. The compression ramp begins $248mm$ (37δ) downstream of the domain inlet and extends $54mm$ (7δ) downstream of the corner. The domain is $100mm$ (15δ) high at the inlet. The width of the flat plate is $203mm$ (30.3δ) wide at the inlet and matches the full width of the wind tunnel in the experiment. The ramp is $153mm$ (22.8δ) wide with aerodynamic fences on either side. The aerodynamic fences start $38.1mm$ (5.7δ) upstream of the corner and have an angle of $\alpha = 30°$.[42] These measurements exactly match those of the configuration detailed in the reference experiment.[30] In the experimental geometry, the aerodynamic fences were $3.18mm$ (0.47δ) thick with a sharp leading edge and a 30° bevel.[42] This geometry has been simplified for the simulation such that the aerodynamic fence is a wedge of angle 0.002° thus providing an aerodynamic fence with effectively no thickness. Errors due to this simplification are not expected to significantly impact the details of the flow as Settles observed little sensitivity to the size and shape of the aerodynamic fences in his experimental investigations.[43] Figures 1a and 1b show the geometry and relevant dimensions from two perspectives with the flow going from left to right in figure 1b. To avoid confusion, we will generally refer to the $x-$, $y-$, & $z-$directions as streamwise, wall normal, and spanwise unless otherwise specified. For reference, we have also performed a calculation of a span-periodic STBLI (SP-STBLI) of the same configuration. The dimensions of the span-periodic domain are identical to that of the 3D domain except for the span-wise direction which is 4.4δ wide. This spanwise extent is twice that of previous span-periodic calculations performed on this configuration.[2,13,14,18,19,32]

The mesh resolution is summarized in table 2. The stream-wise mesh size ranges from $\Delta x^+ = 16$ in the incoming boundary layer to $\Delta x^+ = 8$ at the corner, where $^+$ indicates wall units as calculated from the wall stress at the reference location, $x/\delta = -9$. The wall-normal mesh size ranges from $\Delta y^+ = 0.5$ at the wall to $\Delta y^+ = 16$ at the boundary layer edge. The wall normal spacing is aggressively coarsened away from the boundary layer except for the region of the interaction and recovery, where the spacing of $\Delta y^+ = 16$ is maintained to a point just above the edge of the aerodynamic fence. The span-wise mesh size ranges from $\Delta z^+ = 0.5$ at the aero-fence surface, to $\Delta z^+ = 8$ a distance 1δ from the aerodynamic fence surface. This spanwise resolution is maintained through the center of the domain. In this study the boundary layers on the flat plate, compression ramp, and both sides of the aerodynamic fences are resolved. The resolutions for the span-periodic case are identical to those used by Dawson *et al.*[19] and are given in the table as well. The grid resolution of the 3D calculation is slightly less than that of the span-periodic calculation in the wall-normal direction in the outer boundary layer but identical in all other regions. Figure 2 shows the mesh along the flat plate/ramp center-line for the 3D case.

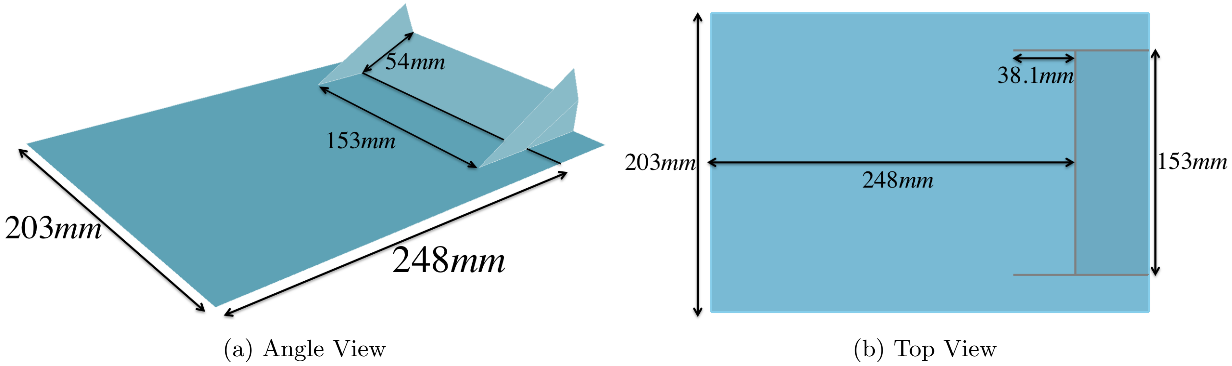

(a) Angle View (b) Top View

Figure 1: Problem geometry.

	Δ_x^+	Δ_y^+	Δ_z^+	N_{Total}
Present - 3D-STBLI - LES	8-16	0.5-16	0.5-8	98.5M
Present - SP-STBLI - LES	8-16	0.5-11	8	18.0M
Wu & Martin[2,13] - DNS	3.4-7.2	0.2-N/A	4.1	21.0M

Table 2: Grid Resolution

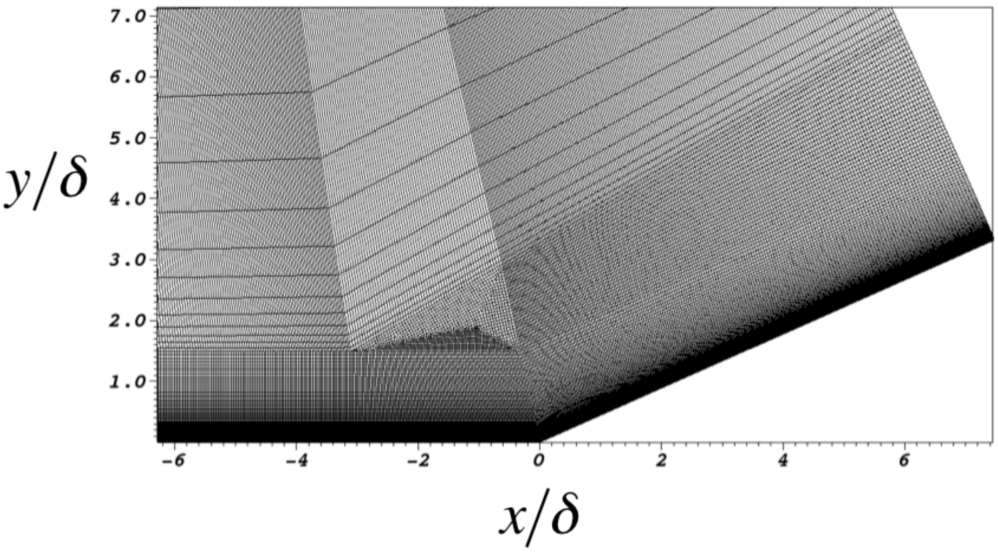

Figure 2: Mesh taken at the $z = 0.0$ plane.

III. Validation

A. Turbulent Boundary Layer

Since the digital filtering inflow generation technique attempts to impose a quasi-physical turbulent boundary layer as the inflow, the boundary layer recovers to a physical state as it develops. It was found by Morgan *et al.*[44] that the digital filtering technique required 15δ for a $M_\infty = 2.28$ turbulent boundary layer to fully recover to equilibrium conditions. Since our Mach number is higher, we have chosen a longer recovery length. We consider the point 9δ upstream of the corner to be our reference location providing a length of 28δ upstream of this reference location over which the boundary layer recovers. It was shown by Dawson *et al.*[19] for a span-periodic calculation of the same conditions, that the boundary layer was fully recovered at the reference location. However, since the mesh resolution in the present study is slightly coarser in the wall-normal direction than that for the span-periodic calculation conducted here, we present comparisons of critical quantities against both the experiment and the span-periodic calculations as validation.

Figures 3a and 3b show the mean stream-wise velocity profile and the van Driest transformed velocity profile, respectively. The reference experimental data[30] and the span-periodic results are shown for reference in both cases. The van Driest velocity profiles are computed by applying the compressible-incompressible transformation of van Driest[45] given by equation 1. The van Driest *Law-of-the-Wall*,[45] given in equation 2, in which $\kappa^* = 0.41$ and $C = 5.2$, is shown for comparison. The mean velocity profiles from both the 3D and span-periodic cases show excellent agreement with the reference experiment. Similarly, the 3D and span-periodic van Driest profiles show excellent agreement with the reference experiment and the van Driest *Law-of-the-Wall.* Van Driest profiles are sensitive to the skin friction therefore the excellent agreement indicates that the skin friction is being accurately predicted by the 3D and span-periodic calculations. The profiles from both the 3D and span-periodic calculations are taken at the streamwise reference location, $x/\delta = -9$ relative to the compression corner.

Figures 4a and 4b show profiles of the Reynolds Stress taken in the undisturbed boundary layer on a linear and logarithmic scale respectively. The four components shown are $u'u'$ (blue), $v'v'$ (red), $w'w'$ (green), and the shear term $u'v'$ (black). The profiles from the span-periodic calculation are shown for comparison. The 3D and span-periodic profiles show excellent agreement with each other except for slightly higher predicted peaks of $u'u'$ and $w'w'$. This slight difference in predicted peak fluctuation values is most likely due to the slightly coarser wall-normal mesh resolution used in the 3D case relative to the span-periodic.

Figures 5a and 5b show profiles of mean and *rms*, respectively, of the scalar quantities pressure, density, temperature, and molecular viscosity. The experimental data of Bookey,[31] at matching conditions, is shown for the mean density profile. The 3D and span-periodic cases show excellent agreement with each other and with the experimental data in the mean profiles. The 3D case shows a slight over-prediction in the *rms* quantities similar to that observed in the Reynolds stress, but the difference is small and most likely due to the slight difference in wall-normal resolution.

$$u^+_{VD} = \int_0 u^+ (\frac{\rho}{\rho_w}) du^+ \tag{1}$$

$$u^+_{VD} = \frac{1}{\kappa^*} \ln y^+ + C \tag{2}$$

B. Interaction

Having established confidence in the quality of our incoming turbulent boundary layer, we turn our attention to the interaction region. Figures 6a and 6b show the wall pressure profile and the skin friction coefficient, respectively. In both cases, the spanwise averaged mean profiles are shown for both the 3D and span-periodic cases. For the 3D case the data is spanwise averaged between $z/\delta = -8$ to 8 which is the spanwise region that is sufficiently free of any disturbances from the presence of the aerodynamic fences as will be discussed in section IV. The data is averaged over a time of $\tau = tu_\infty/\delta = 900$ which is more than sufficient to acquire converged statistics for these quantities. Despite the fact that flows of these types are generally considered to be statistically homogeneous in the spanwise direction, there is significant spanwise inhomogeneity of the flow, particularly in the interaction and recovery regions where stable spanwise varying structures can exist.[20, 21, 25] Since experimental data is usually taken at only a single spanwise location, it is unfair to compare numerical spanwise averaged mean wall profiles with mean experimental profiles as pointed out

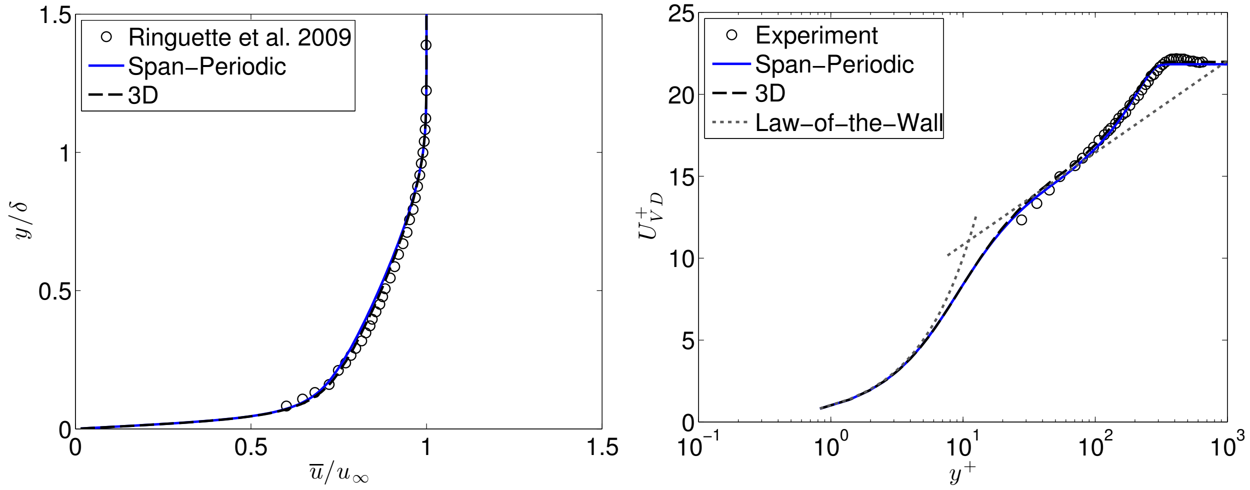

(a) Mean Streamwise Velocity

(b) van Driest Transformed Velocity

Figure 3: Mean stream-wise velocity profile (left) and van Driest transformed velocity profile (right). Profiles taken in the undisturbed incoming boundary layer at $x/\delta = -9$. Experimental[30] results, the *Law-of-the-Wall*[45] theory, and span-periodic results are shown for comparison.

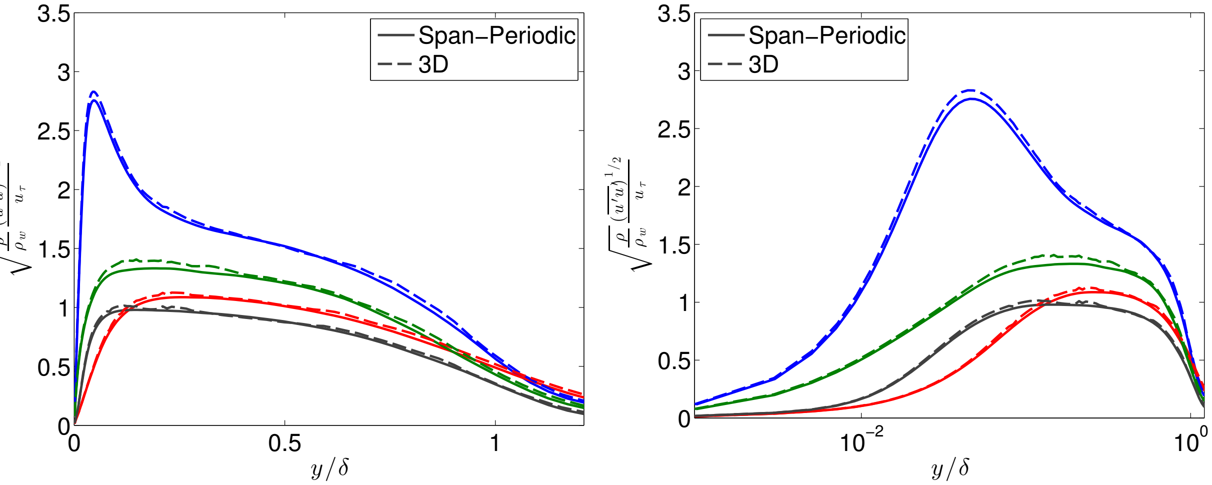

(a) Linear

(b) Logarithmic

Figure 4: Profiles of Reynolds Stress taken in the undisturbed incoming boundary layer at $x/\delta = -9$. Profiles of $u'u'$ (BLUE), $v'v'$ (RED), $w'w'$ (GREEN), and $u'v'$ (BLACK) are shown. Results from the span-periodic case are shown for reference.

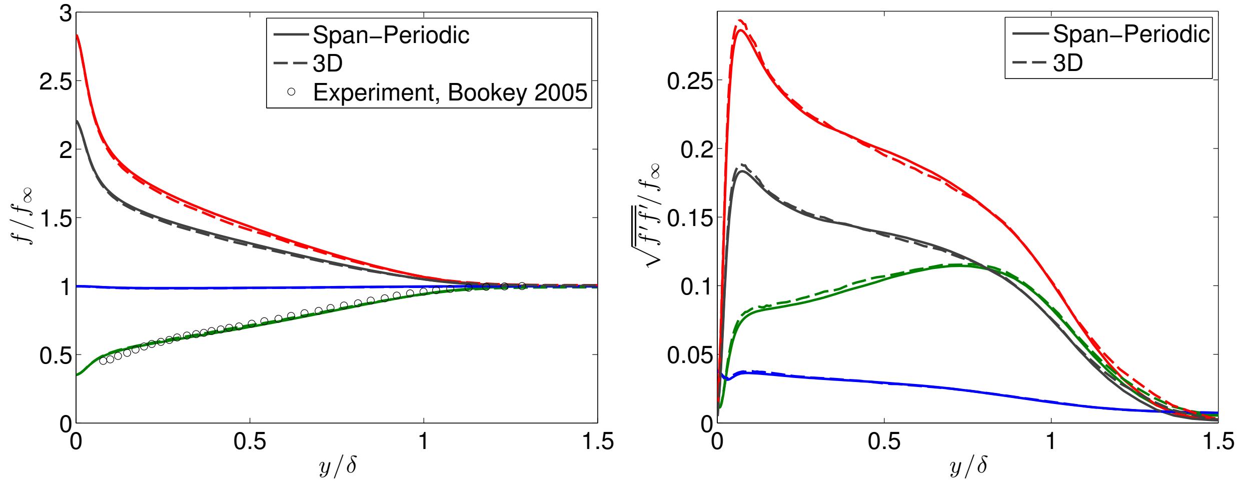

(a) Linear

(b) Logarithmic

Figure 5: Profiles of mean and *rms* scalar quantities taken in the undisturbed incoming boundary layer at $x/\delta = -9$. Pressure (BLUE), density (GREEN), temperature (RED), and molecular viscosity (BLACK) are shown. Span-periodic results and experimental data[31] (where available) are shown for comparison.

by Loginov *et al.*[25] This issue will be discussed in more detail in section IV. To highlight the spanwise inhomogeneity of the flow, the spanwise minimum and maximum values (taken between $z/\delta = -8$ to 8) are plotted to define an envelope of possible mean values across the span of the compression ramp. We observe that there is little mean spanwise variation in the pressure and that the 3D solution shows excellent agreement with the experiment through the domain. The span-periodic case shows a slightly early pressure rise compared with the experiment, however the plateau and recovery region agree with the experimental data. The spanwise variation in the skin friction coefficient is significantly larger than that observed in the wall pressure, especially in the separated and recovery regions. The spanwise min/max envelope encompasses both the separation point and reattachment point observed in the experiment. The span-periodic case, again shows a premature start to the interaction in the form of an early drop in skin friction and separation relative to the experiment and 3D calculation. The span-periodic case agrees well with the experimentally observed recovery point and the 3D case through the recovery region. The large variation of skin friction coefficient in the spanwise direction suggests that wall pressure may be a more appropriate quantity to validate against in the absence of experimental data at multiple spanwise locations.

The over-prediction in interaction size is shown in contours of streamwise velocity, wall normal velocity, and Reynolds stress in figure 7. Although the qualitative behavior is consistent between the 3D solution and the span-periodic solution, the interaction is consistently smaller in the 3D solution. This small but consistent over-prediction in the size of the interaction by the span-periodic case may be due to the spanwise domain size being too small resulting in a confinement effect. Since previous high-fidelity calculations of this flow geometry[2,13,14,18,19,32] have used relatively small spanwise domain sizes ($L_z = 2.2\delta$), it is important to keep in mind the effects that this computational cost driven choice can have on the underlying physics, especially when validating against experimental results.

IV. Results

A. Characterization

One of the primary objective of this investigation is to study the three-dimensional aspects of a compression ramp interaction with flow confining aerodynamic fences. Although generally idealized as a span-periodic flow, the presence of the aerodynamic fences will always be non-negligible, at least in the regions near the aerodynamic fences. To characterize the effects of the aerodynamic fence on the interaction, we consider mean velocity and Reynolds Stress contours on a streamwise normal plane located at $x = -0.5\delta$ as shown

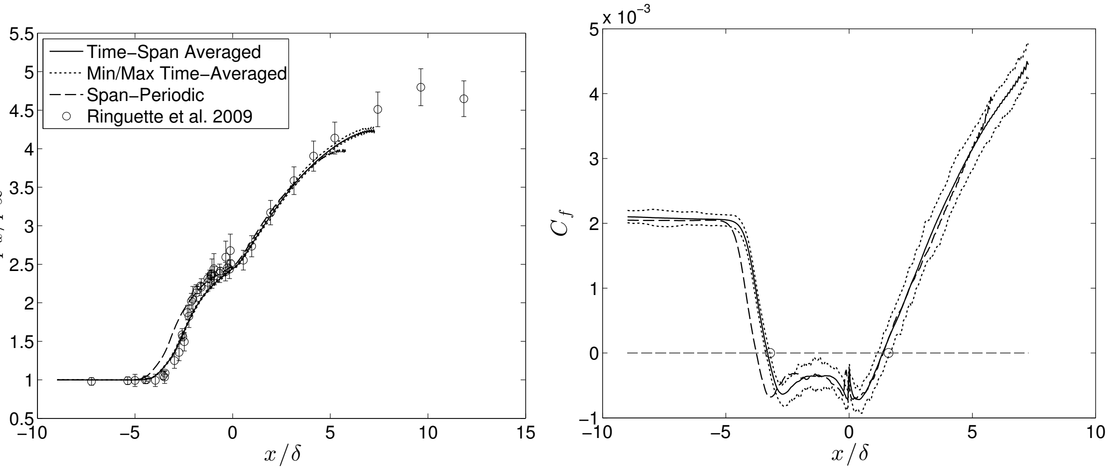

(a) Wall-Pressure

(b) Skin Friction Coefficient

Figure 6: Wall pressure (LEFT) and skin friction coefficient (RIGHT). Experimental results of Ringuette et al. 2009[30] and span-periodic results shown for comparison. The Min/Max envelope is defined as the minimum and maximum values in the spanwise direction at each streamwise location.

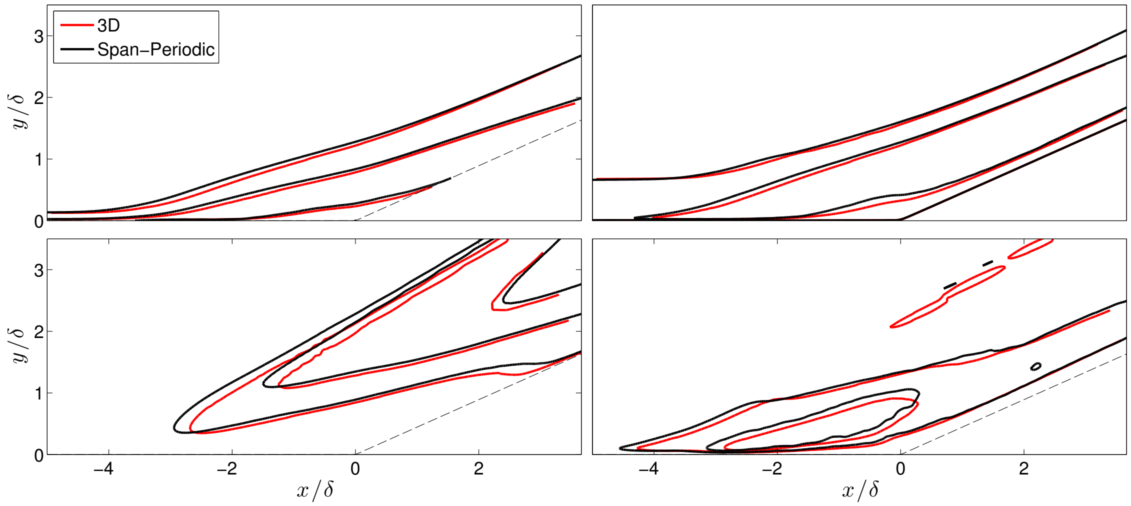

Figure 7: Contours of spanwise averaged mean streamwise velocity (TOP-LEFT), wall normal velocity (BOTTOM-LEFT), $u'u'$ (TOP-RIGHT), and $u'v'$ (BOTTOM-RIGHT) for the 3D calculation (RED) and the spanwise-periodic calculation (BLACK). In the three-dimensional case the data was averaged between $z/\delta = -8$ and 8. The streamwise velocity contours shown are $\overline{u}/c_\infty = 0.0$, 1.0, & 2.0. The wall-normal velocity contours shown are $\overline{v}/c_\infty = 0.25$, 0.5, & 0.75. The streamwise velocity fluctuation intensity contours shown are $\sqrt{\overline{u'u'}}/u_\infty = 0.05$ & 0.15. The Reynolds shear stress contours shown are $\overline{u'v'}/u_\infty^2 = -0.004$ & -0.002.

in figure 8. This location is in the middle of the separated region and the $\overline{u} = 0.0$ contour is shown in the streamwise velocity plot to highlight the region of reversed flow. At this streamwise location, the aerodynamic fence is 3.02δ high. The field of view is restricted to highlight the $-z$ aerodynamic fence region only. The aerodynamic fence is located on the left side of each plot and the horizontal coordinate has been shifted such that its origin is at the aerodynamic fence. The mean velocity is shown in the top row, the diagonal components of the Reynolds Stress in the second row and the off-diagonal components of the Reynolds Stress in the third row of the figure. The streamwise velocity shows a large region of reversed flow near the wall as expected but also shows a region of significantly decreased streamwise velocity along the aerodynamic fence as the flow is slowed by the adverse pressure gradient due to the shock. There is actually a small region of reversed flow, defined here as flow in the negative $x-$direction, near the top of the aerodynamic fence. The wall normal and spanwise velocities show a pair of high and low velocity regions near the fence roughly 1.25δ from the wall indicative of a vortex in the streamwise direction. The mean velocity of the interaction is relatively undisturbed by the presence of the aerodynamic fence outside of roughly 1.5δ from the fence. The limited range that the aerodynamic fence impacts the flow allows us to treat the center of the flow as nominally two dimensional. Within this region, however, the mean flow of the interaction is severely distorted. All three of the diagonal components of the Reynolds Stress show peak values in the shear layer above the separation bubble. High values of all Reynolds Stress components are observed in the region surrounding the “bubble” of retarded flow on the surface of the aerodynamic fence.

To better understand the flow organization near the aerodynamic fence we consider the mean pressure, dilatation, and Q criterion as shown in figure 9 on the same $x/\delta = -0.5$ plane as in figure 8. Based on the dilatation field (middle) we see that the primary shock is undisturbed by the aerodynamic fence outside of 1.25δ from the aerodynamic fence surface but turns sharply upward at this point where it joins with the secondary shock generated by the aerodynamic fence leading edge. The primary shock continues to penetrate into the aerodynamic fence boundary layer for roughly 0.5δ past the point of intersection with the secondary shock. The primary shock quickly diffuses as it penetrates deeper into the aerodynamic fence boundary layer. The pressure field (LEFT) is consistent with the primary and secondary shock structure indicated by the dilatation, but shows a region of intermediate pressure between the pre- (low pressure) and post- (high pressure) shock regions. There is a small region of low pressure indicative of a vortex at about 1.25δ up the aerodynamic fence. This is supported by the presence of a strong positive region of Q criterion (RIGHT) in the same location. The presence of this vortex is also supported by the wall normal and spanwise velocity fields in figure 8. A weaker, secondary vortex is present just above the primary vortex and slightly closer to the aerodynamic fence surface. Figure 10 shows contours of mean pressure and Q criterion on a $z-$normal plane a distance of 0.15δ from the aerodynamic fence. We observe that the vortex indicated by the region of positive Q in figure 9 actually begins near the corner and is lifted up and away from the flat plate/ramp surface. The vortex persists a significant distance downstream of the corner. This strong vortex is evident in the pressure field as well, as a region of decreased pressure along the position of the vortex. A weaker, secondary vortex appears above the primary vortex.

To get a more comprehensive view of the three-dimensional flow organization near the aerodynamic fence we consider, in figure 11, the $p/p_\infty = 1.2$ iso-surface to highlight the location of the shock,[46] and the $Q = 5.5$ iso-surface to highlight coherent vortices. The flat plate and ramp surface are colored by mean pressure. The domain is limited to $x/\delta = -6$ to 6 and $z/\delta = -12$ to -8. Away from the aerodynamic fence, the primary shock is undisturbed by the presence of the aerodynamic fence and bends normal to the flat plate as the shock foot approaches the surface. As it approaches the aerodynamic fence it joins with the shock off of the leading edge of the aerodynamic fence and curves away from the flat plate/ramp surface. The shock foot moves upstream near the aerodynamic fence. The iso-surface of Q indicate two stable vortices near the aerodynamic fence, consistent with that observed in figures 9 and 10. The primary vortex developes in the interaction and runs parallel to the ramp along the surface of the aerodynamic fence all the way to the outflow boundary. The secondary vortex is weaker and appears to dissipate before leaving the domain.

To characterize the three dimensional flow further, we consider the three-dimensional streamlines shown in figure 12. The flat plate/ramp are colored by p/p_∞ as is the plane in line with the aerodynamic fence surface. The streamlines are seeded at twenty locations evenly spaced between $z/\delta = -11.3$ and -10 at a height $y/\delta = 0.01$, at the three streamwise locations of $x/\delta = -2$ (BLUE), -1 (WHITE), and 0 (RED). A number of features are highlighted by these streamlines. There exists a large reversed flow near the aerodynamic fence upstream of the blue seed points which then turns away from the aerodynamic fence and flows back downstream, forming a large region of rotating flow. A region of significant reversed flow is also

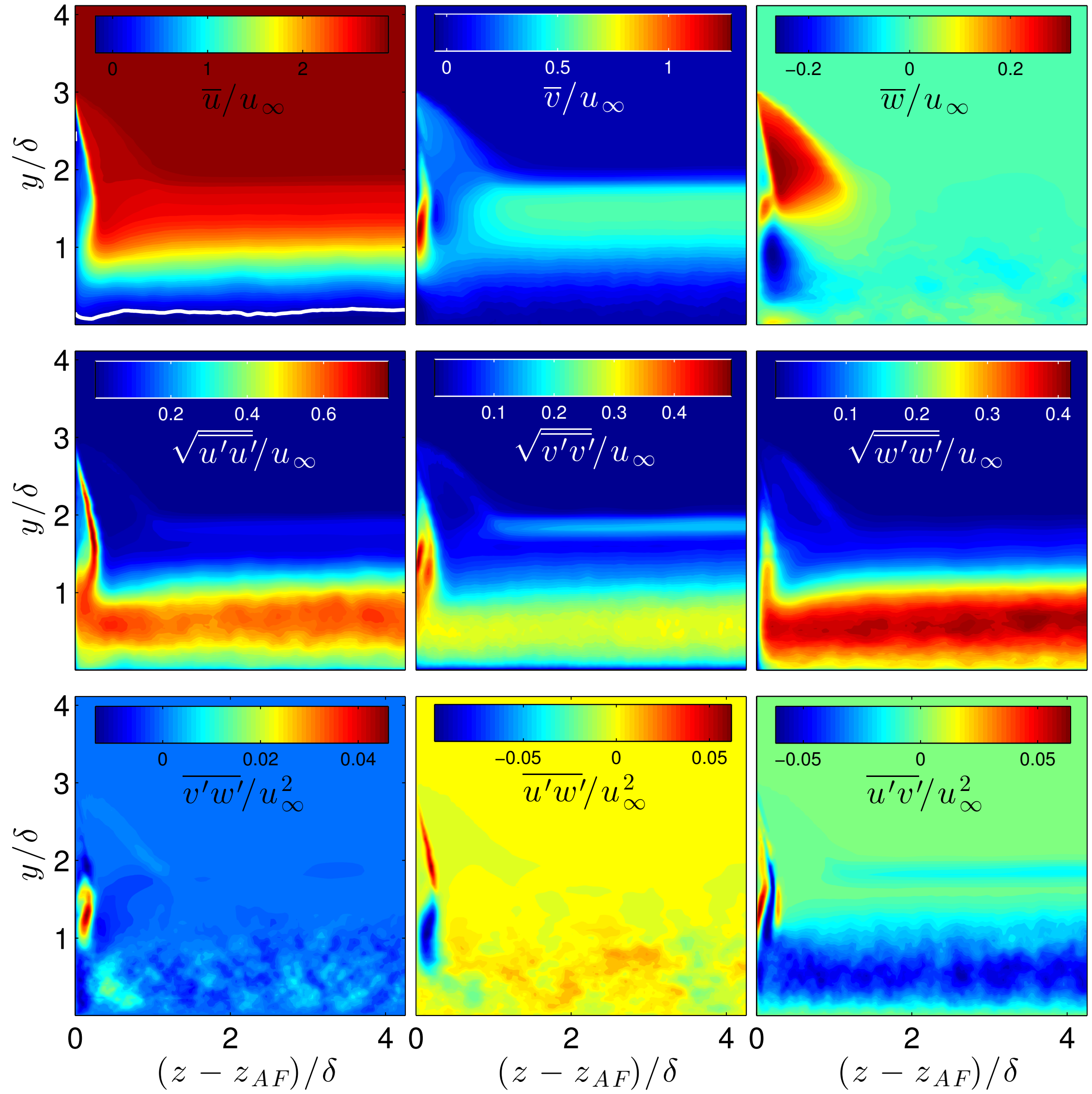

Figure 8: Contours of mean velocity (Top Row), diagonal components of Reynolds Stress (Middle Row), and off-diagonal components of Reynolds Stress (Bottom Row), taken at the $x/\delta = -0.5$ plane near the $-z$ aerodynamic fence. The horizontal coordinate has been shifted such that the origin is at the location of the aerodynamic fence.

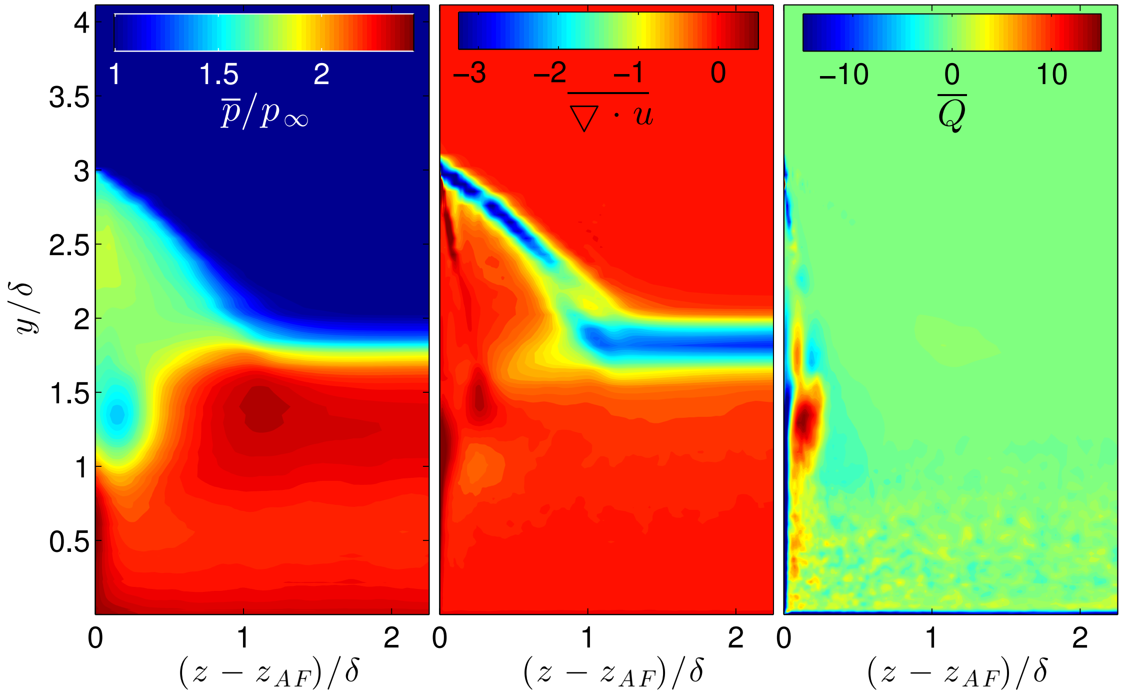

Figure 9: Contours of mean pressure (LEFT), Dilatation (MIDDLE), and Q criterion (RIGHT) on the $x/\delta = -0.5$ plane.

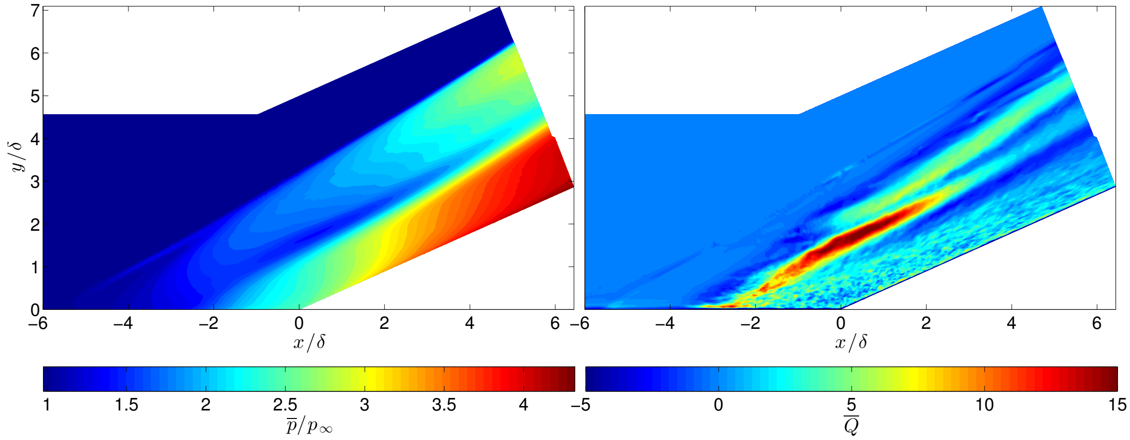

Figure 10: Contours of mean pressure (LEFT) and Q criterion (RIGHT) on the $z-$normal plane 0.15δ from the aerodynamic fence.

observed on the surface of the aerodynamic fence which appears to be the continuation of the recirculation region on the flat plate surface. Near the corner, just upstream of the red seed points, the flow movies in the upstream direction before lifting off of the flat plate surface, reversing directions, and being carried downstream. The primary vortex visualized in figure 11 is observed as a twisting bundle of streamlines which is formed primarily out of the large rotating flow region which begins upstream of the blue seed points. The secondary vortex is also visible as a smaller vortex above and slightly behind the primary vortex. The blue streamlines are divided into two main paths. The first is to flow into the large recirculating flow and eventually into the primary vortex. The second is to flow downstream, joining the secondary vortex. The white streamlines are also divided into two main paths, the first is into the recirculating flow and eventually into the primary vortex, while the second is to be carried downstream. Similarly the red streamlines flow either into the recirculating region or are carried downstream. The streamlines highlight that the large recirculating region eventually becomes the primary vortex as it is turned downstream.

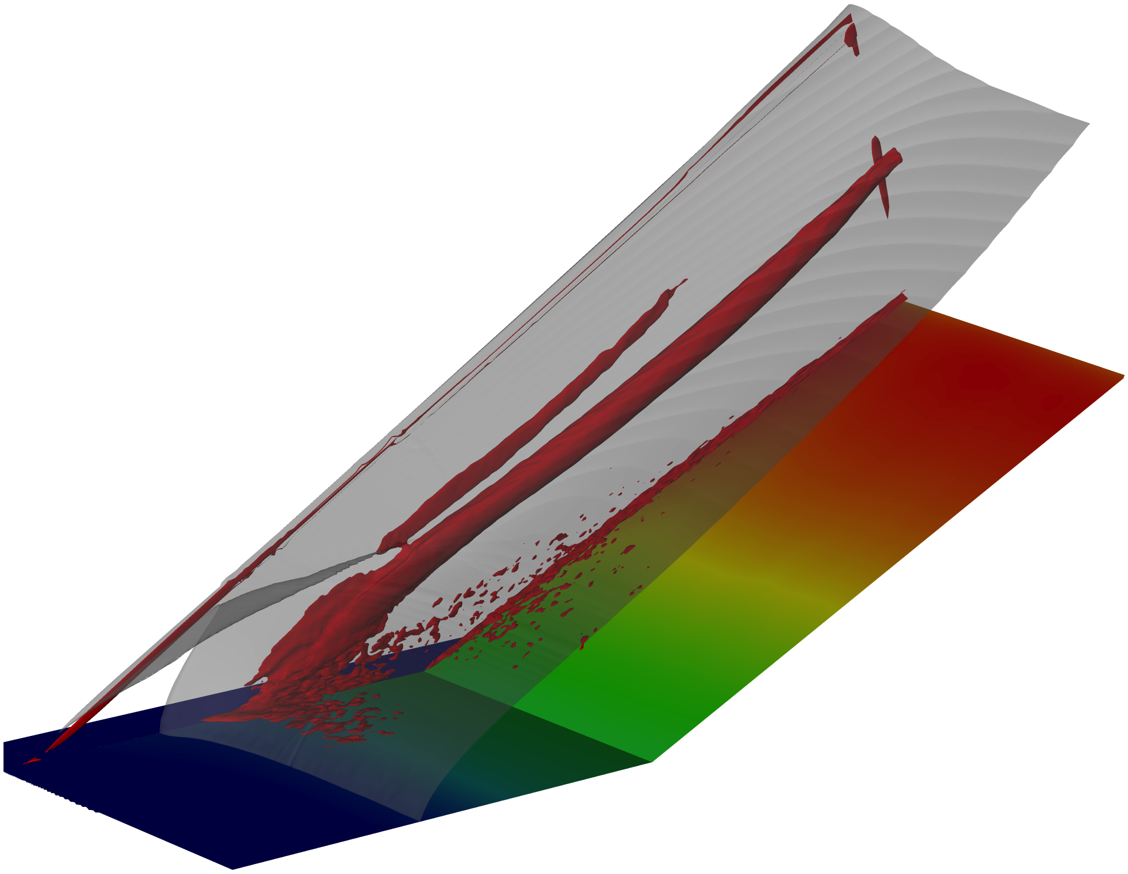

Figure 11: Iso-surfaces of Q criteria, $Q = 5.5$ (red), and pressure, $p/p_\infty = 1.2$ (semi-transparent grey). Pressure is shown on the surface of the flat plate/ramp.

B. Spanwise Inhomogeneity

When considering STBLI with 2D geometries, the assumption is almost always made that the turbulent flow is statistically homogeneous in the spanwise direction. This assumption allows for averaging of statistics in the spanwise direction which decreases cost by providing statistical convergence in fewer time steps. Additionally, experimental results are usually acquired at a single spanwise location, with little consideration as to what specific spanwise location is used as long as it is sufficiently unaffected by the influence of wind tunnel walls, model edges, or aerodynamic fences. To achieve this, the center line is usually chosen, though not always. As is shown in figure 6b the skin friction coefficient shows a significant difference between the mean spanwise minimum, maximum, and average values. The time history of the skin friction is more than sufficient to achieve converged average statistics, therefore the significant variation between the spanwise minimum and

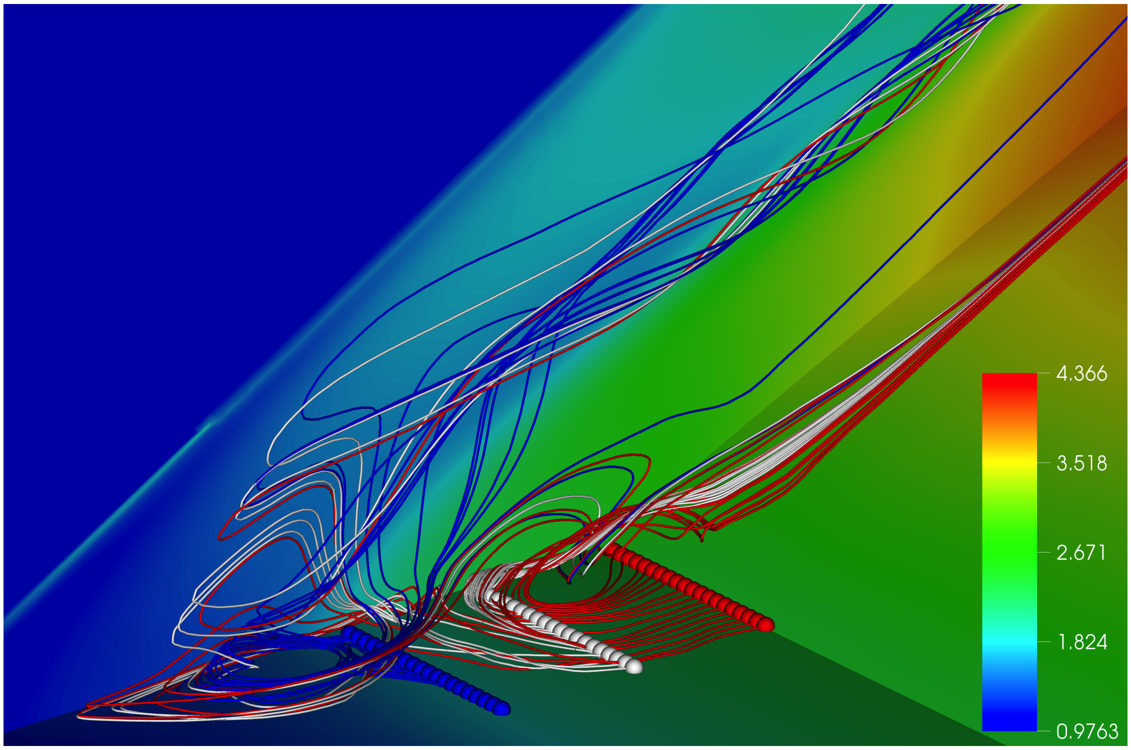

Figure 12: Streamlines through mean corner flow. Three sets of 20 streamlines are seeded between $z/\delta = -11.3$ to -10 at a height of $y/\delta = 0.01$. The three sets are seeded at $x/\delta = -2$(BLUE), $x/\delta = -1$(WHITE), & $x/\delta = 0$(RED). The mean pressure is shown on the surface of the flatplate/ramp as well as the z location of the aerodynamic fence.

maximum mean values indicates regions of high and low skin friction which are stable over time scales much longer than those usually associated with the problem.

We can visualize these spanwise inhomogeneities in the form of contours of skin friction coefficient shown in figure 13 and streamlines taken at the wall shown in figure 14. In figure 13 the region of reversed flow is indicated by the thin black line while the aerodynamic fences are indicated by vertical black lines at $z/\delta = \pm 11.42$. Away from the aerodynamic fences, the separation line has a mean location of $x_{sep}/\delta = -3.3$, and shows some small variation in position of about 0.1δ. Near the aerodynamic fence, the separation lines move downstream by roughly 0.5δ before reaching the aerodynamic fence far upstream of the mean separation point. This distortion of the separation line coincides with the strong recirculation region observed in figure 12. Away from the aerodynamic fence, the reattachment line has a mean location of $x_{reat}/\delta = 1.4$, and shows significant variation in location of about 0.25δ from the mean. Downstream of the reattachment location, the skin friction shows significant variation in the spanwise direction. The skin friction in the separated region shows similar spanwise variation. The variations appear to have a characteristic spanwise width of roughly 2.0δ though smaller and larger length scales are also present. A similar pattern has been observed in previous work[20, 21, 25] in which it has been proposed that Görtler-like vortices are the cause of spanwise inhomogeneities.

We can get a different view of the flow behavior near the wall by looking at streamlines calculated from the velocity field in the first cell off the wall in figure 14. This visualization is somewhat analogous to oil flow visualization used in experimental investigations. The streamlines are seeded with a single row of 200 points evenly spaced in the incoming flow ($x/\delta = -5.9$) as well as 1000 points evenly spaced in the spanwise direction but randomly distributed between $x/\delta = 1.0$ to 1.35 to capture the reattachment line. Upstream of the interaction, the streamlines show essentially no deviation from a pure streamwise motion except for the regions near the aerodynamic fence which are located at the leftmost and rightmost boundaries of the figure. The distortion of the separation line near the aerodynamic fence is again consistent with the presence of a large recirculation region indicated by figure 12. The streamlines from the inflow and the separation bubble converge at the separation line. The variation in separation position appears more pronounced than that indicated by figure 13. In both the separated region and the recovery region, the streamlines converge into bundles oriented in the streamwise direction. This alternating pattern of convergent and divergent streamlines is indicative of the alternating up-wash and down-wash regions of pairs of counter rotating vortices, such as Görtler-like vortices. Near the aerodynamic fence, we observe significant deviation from the mid-region behavior.

As we observed in figure 13, the separation and reattachment lines show very different behavior. This is clearly shown in the location of separation, reattachment and separation length in figure 15a. The reattachment point and separation length show large deviations with a characteristic length of roughly 2δ and the separation point shows only small deviations, most less than 0.05δ, with a distinctly smaller characteristic spanwise length scale. The wavelength of the spanwise inhomogeneous structures of 2δ observed in figures 13, 14, and 15a is consistent with the wavelength of Görtler-like vortices observed experimentally by Floryan.[47] By taking the energy spectra of the separation point and reattachment point signal between $z/\delta = -8$ to 8 shown in figure 15b, we can extract the differences in characteristic lengths based on their energy content. The spectra above $\kappa_z = 1.4$ corresponding to $L_z/\delta = 0.7$ shows little difference in magnitude between the separation and reattachment points. However, below this value the reattachment location spectra has a value much larger than the separation point spectra. At around $\kappa_z = 0.6$, or $L_z/\delta = 1.7$, the reattachment spectra is nearly two orders of magnitude larger than that of the separation point spectra. This peak is close to the value 2.0δ estimated from figures 13 and 15a. Both spectra begin to decrease below $\kappa_z = 0.3$, or $L_z/\delta = 3.3$.

Alternatively we can observe the the spanwise inhomogeneity in the skin friction coefficient as a function of spanwise position. Plotted in figure 16a are the spanwise profiles of skin friction coefficient at five streamwise stations, from top to bottom, $x/\delta = -8$, -3.3, -0.5, 1.4, & 4.0 corresponding to the undisturbed inflow, the separation point, the separation bubble, the reattachment point, and the recovery region. The profiles plotted have been averaged in time only, though the time and spanwise averaged value is included for reference. The profile taken at the inflow shows the smallest magnitude variation as well as the smallest characteristic length scale. The profile from the separation location shows variations that are slightly larger in amplitude than the inflow profile, and has a similar characteristic wavelength. In the separation bubble, the skin friction begins to exhibit larger amplitude variation and with slightly longer characteristic wavelengths relative to the upstream profiles. The profiles taken at the reattachment location and recovery region exhibit

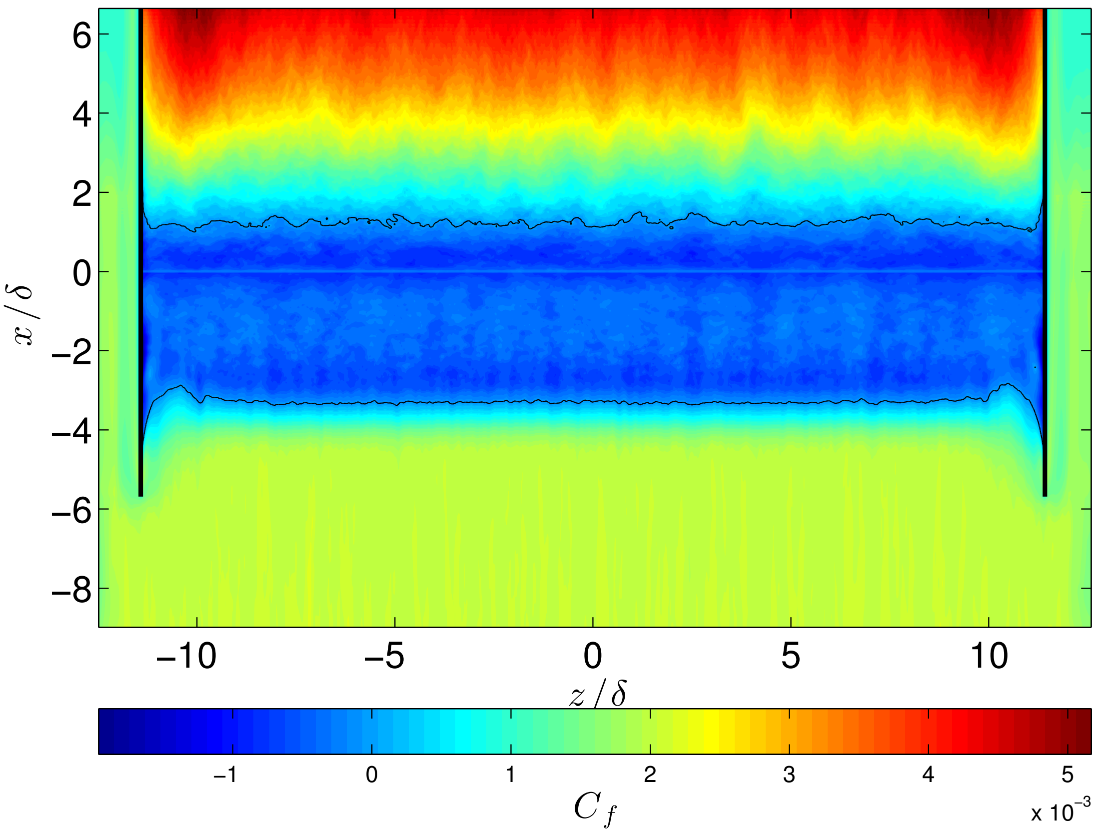

Figure 13: Contours of Skin Friction Coefficient on the flat plate and ramp surfaces.

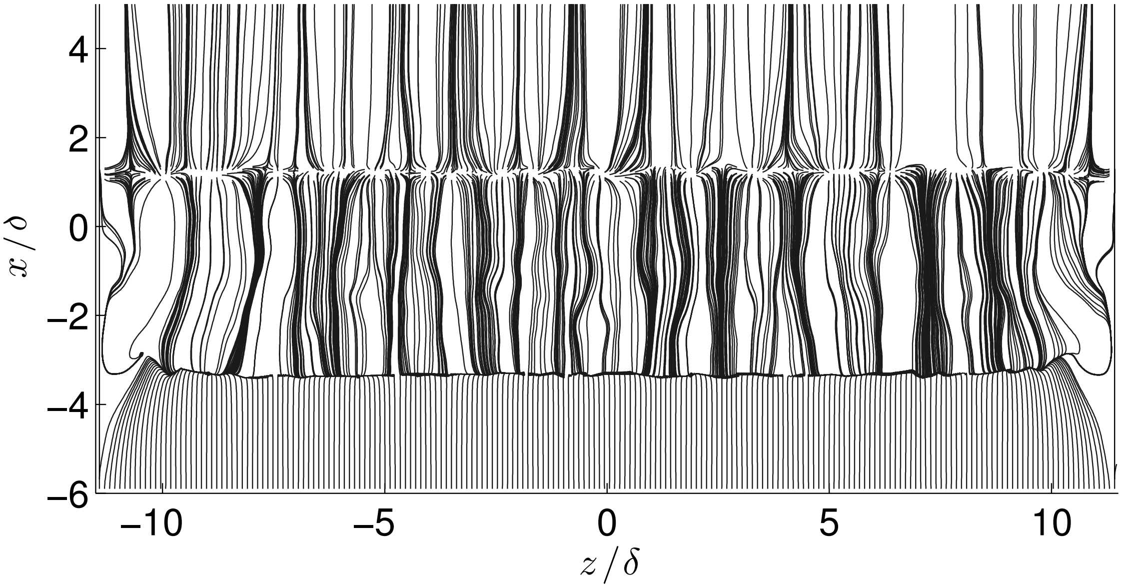

Figure 14: Streamlines along flat plate and ramp surfaces.

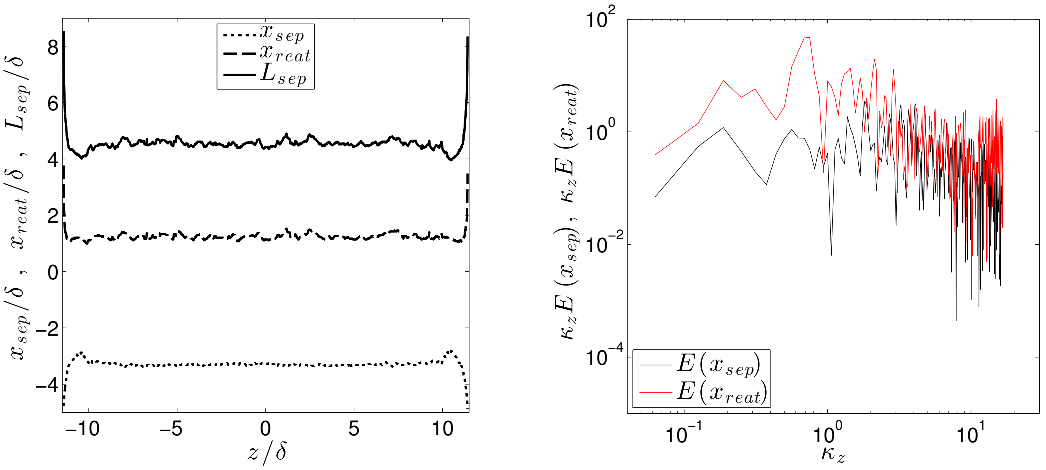

(a) Position/Length

(b) Energy Spectra

Figure 15: Separation/Reattachment point and separation length (LEFT). Compensated energy spectra of separation and reattachment point as a function of spanwise wavenumber.

the largest variation amplitude and exhibit a characteristic wavelength of slightly less than 2.0δ consistent with the reattachemnt point spectra in figure 15b. Additionally, some, though not all, of the devations from the mean value match between the reattachment point and the recovery region indicating a coherent effect which persists downstream. A more complete view of the relavent lengthscales can be observed in figure 16b which showns the compensated energy spectral density of the instantaneous skin friction profiles as a function of spanwise wavenumber, κ_z and streamwise location. The spectra are averaged in time. Upstream of the interaction, the peak energy occurs at $\kappa_z = 3/\delta$, or $L_z = 0.3\delta$. Beginning at the separation point, peak energy increases in amplitude and shifts to lower wavenumber of about $\kappa_z = 1/\delta$. After the corner the peak energy shifts to an even lower wavenumber of $\kappa_z = 0.6/\delta$ or $L_z = 1.7\delta$. The energy peak remains at this wavenumber for the remainder of the domain, though the signal becomes significantly more broadband as it recovers from the interaction.

The presence of Görtler-like vortices is certainly suggested from the nature of the spanwise inhomogeneities. A turbulent analogue for the Görtler number given by Tani[48] is given as

$$G_T = \frac{\theta}{0.018\delta^*}\sqrt{\frac{\theta}{R}} \tag{3}$$

where R, the radius of curvature of the flow, is given by

$$R = \frac{1}{\kappa} \tag{4}$$

and κ is the two-dimensional curvature of the flow, given as[49]

$$\kappa = \frac{\left(u^2\frac{\partial v}{\partial x} - v^2\frac{\partial u}{\partial y} + uv\left(\frac{\partial v}{\partial y} - \frac{\partial u}{\partial x}\right)\right)}{\left(u^2+v^2\right)^{3/2}} \tag{5}$$

and can be calculated entirely from the velocity field.

Figure 17a shows contours of the turbulent Görtler number as computed from the mean velocity field at the centerline via equations 3 through 5. The critical Görtler number of 0.6[50] is shown as a solid white contour. Also shown is a streamline starting at $(x, y) = (-6\delta, 0.05\delta)$ as a dashed white line. The upper limit of the color scale has been artificially limited to prevent the extremely high values in the shear layer from drowning out the details elsewhere. The turbulent Görtler number has high values along the separation and reattachment shocks as well as the region in and above the separation bubble and shear layer where the flow is either turned back on itself or deflected over the separation bubble. The turbulent Görtler number

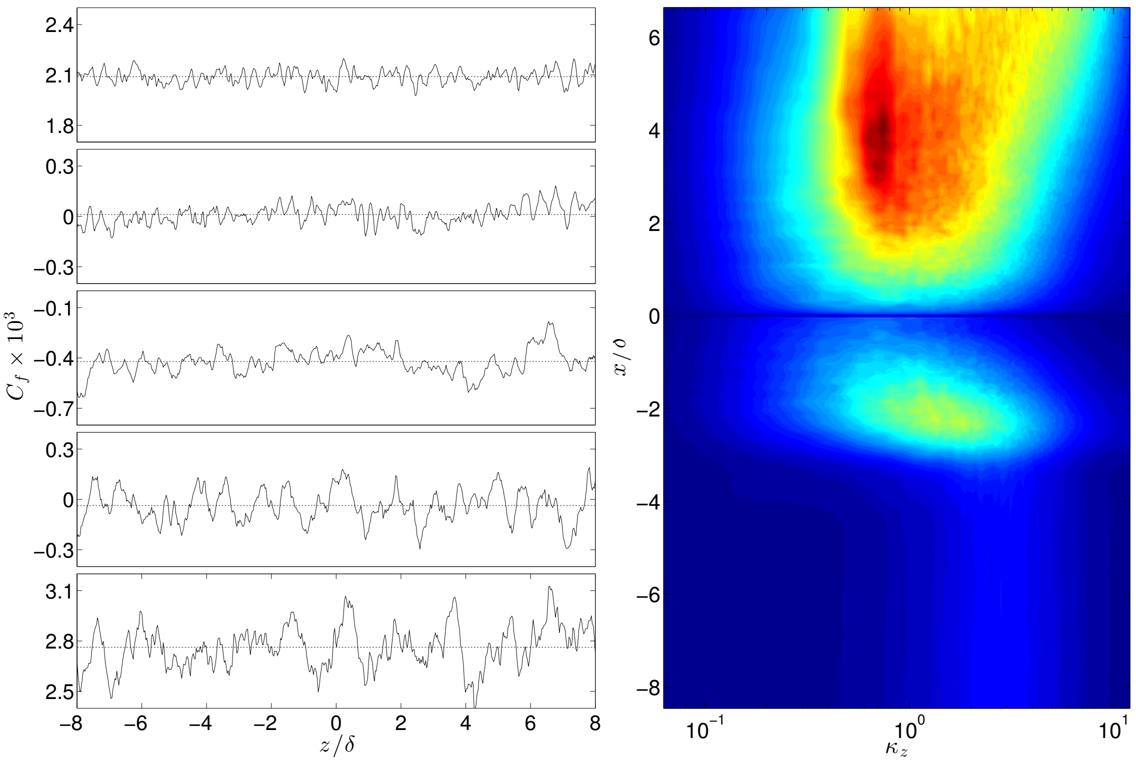

(a) Skin Friction Coefficient

(b) Energy Spectra

Figure 16: Skin friction coefficient as a function of spanwise position (LEFT) taken at 5 streamlines locations of, from top to bottom, $x/\delta = -8$, -3.2, -0.5, 1.5, & 4.0. Contours of compensated energy spectra of skin friction coefficient as a function of spanwise wave number, $\kappa_z\, E(C_f)$.

decreases as the boundary layer recovers and the flow straightens. The regions around the shock system, separation bubble, and reattachment all have values higher than the critical value, above which Görtler vortices are likely to form. The turbulent Görtler number along the indicated streamline is shown in figure 17b. Along the streamline, the critical value is exceeded through the entire interaction with the highest value achieved roughly at the shock foot location.

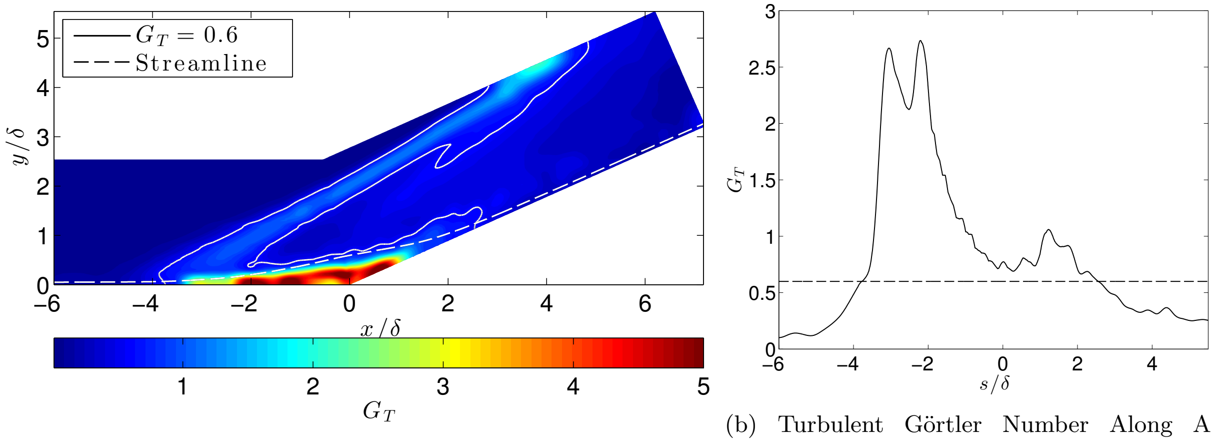

(a) Turbulent Görtler Number Contours

(b) Turbulent Görtler Number Along A Streamline

Figure 17: Contours (LEFT) of Turbulent Görtler Number with critical threshold value indicated (SOLID LINE). A streamline originating at $(x, y) = (-6\delta, 0.05\delta)$ is shown (DASHED LINE). The Turbulent Görtler Number along the streamline (RIGHT) with critical threshold value indicated (DASHED LINE).

We can observe the presence of the vortices directly as shown in contours of streamwise, wall normal, and spanwise perturbation velocities, and streamwise vorticity in figure 18. The contours are taken in the $\xi-$normal plane at $\xi/\delta = 1.8$, where ξ is the direction parallel to the ramp surface. The $x-$ & $y-$ velocities have been transformed to align with the ramp aligned (ξ, η) direction. The flow field has been filtered with a Gaussian filter of width 0.2δ to reduce noise in the data. For the streamwise and wall normal velocities, the spanwise average (from $z/\delta = -8$ to 8) value is subtracted from the velocity resulting in the perturbation velocity. Since the mean spanwise velocity should be zero everywhere, it is its own perturbation value. The range of $z/\delta = 1$ to 6 was selected to focus on and highlight the structures observed. The streamwise velocity (top) shows clear alternating positive and negative regions of roughly 2.0δ in width per pair. The magnitude of these perturbations in the unfiltered velocity field is up to 3% of the free stream velocity. The wall normal velocity (second from top) shows a similar alternating pattern of positive and negative values that are aligned with, but opposite in sign to, the streamwise velocity pattern. This indicates that the regions of high streamwise velocity are due to higher momentum fluid being drawn down from the outer boundary layer and the regions of lower velocity are due to lower momentum fluid being drawn up from the inner boundary layer in a manner consistent with the up-wash and down-wash caused by pairs of counter rotating streamwise aligned vortices. The spanwise velocity (second from bottom) shows two rows of alternating positive and negative velocity regions with the top layer having a smaller magnitude than and opposite sign to the bottom layer. These positive and negative velocity regions are of similar spanwise width to those observed in the streamwise and wall normal velocity fields but are aligned with the regions between the high and low regions of the streamwise and wall normal velocities. This checkerboard pattern of positive and negative spanwise velocity indicates that beneath regions of high streamwise velocity the flow is drawn down and diverges at the wall, and beneath regions of low streamwise velocity the flow converges and is drawn up from the wall. These patterns in the velocity field are all consistent with the streamwise vorticity field (bottom) which shows an alternating pattern of positive and negative streamwise vorticity of width equal to roughly 2δ per pair aligned with the gaps between the regions of high and low streamwise velocity.

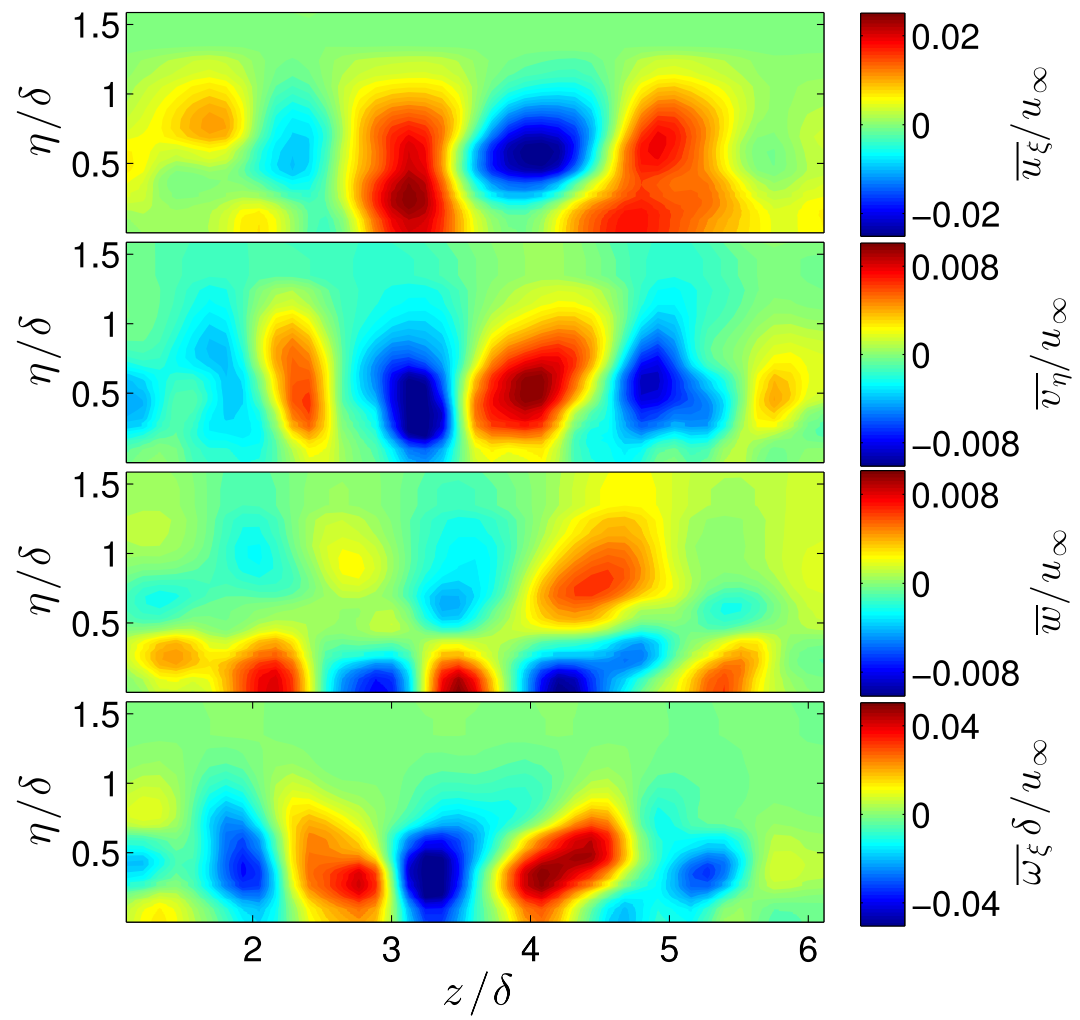

Figure 18: Contours, from top to bottom, of streamwise velocity, wall normal velocity, spanwise velocity, and streamwise vorticity. The streamwise and wall normal velocities and streamwise vorticity have been transformed to align with the angle of the ramp rather than the (x, y, z) Cartesian coordinates and the vertical axis is the distance from the ramp, η/δ. The fields have been filtered in the wall normal and spanwise directions with a Gaussian filter of width 0.2δ to reduce noise.

C. Low-Frequency Unsteadiness

The low-frequency unsteadiness of STBLI has been studied extensively using both experiment and computation as an investigative tool. The cost of high fidelity computational approaches has limited their size and forced both the assumption of spanwise periodicity and narrow spanwise domain sizes. The quality and value of previous studies has been tremendous in furthering our understanding of key aspects of LFU in STBLI. Their limitations, however, leave important questions unanswered, including the effect the presence of three-dimensional flow features has on the nature of LFU and how restrictive spanwise domain sizes effect the low frequency dynamics of the system. We know that insufficient spanwise domain sizes can cause an over-prediction of separation length and so it us not unreasonable to venture that the same confinement affects LFU.

A time history of $\tau = tu_\infty/\delta = 900$ has been collected at intervals of $\Delta\tau = 0.174$. Figure 19 shows the time history of wall pressure taken along the centerline at three streamwise locations, the incoming boundary layer $x/\delta = -9$ (top), the separation location $x/\delta = -3.3$ (middle), and the reattachment location $x/\delta = 1.4$ (bottom). The raw signal is shown in grey, while a low pass filter signal, of filter width $St = 0.02$, is shown in black. The upstream signal shows only high frequency fluctuations. The separation point shows significant low frequency fluctuations on the order of $\tau = 50$ to 150. Addtionally the high frequency fluctuations observed in the upstream flow appear much less at the separation point. The reattachment signal also shows significant low frequency fluctuations as well as significant high frequency fluctuations of a characteristic magnitude much greater than the other two locations. Figure 20a shows contours of compensated power spectral density of wall pressure fluctuations. The horizontal axis is the Strouhal number, $St = f\delta/u_\infty$, while the vertical axis is the x-coordinate. The spectra are averaged in the spanwise direction in the range $z/\delta = -8$ to 8. At each streamwise location, the spectra are normalized by the total energy. The spectra are binned into 25 logarithmically spaced frequency bins. Three streamwise positions are highlighted with horizontal dashed lines. These are, from bottom to top, the undisturbed incoming boundary layer, the location of peak low-frequency content, and the reattachment point. Four characteristic frequencies of the system are highlighted with vertical dashed lines. These are from right to left, the boundary layer characteristic frequency $St_{BL} = 1$, the convective frequency, St_{conv}, the Lagrangian decorrelation frequency St_{LDT}, and the eddy turnover frequency St_{ET}. The incoming boundary layer shows purely high frequency content with essentially no energy in frequencies below St_{LDT}. Just upstream of the separation point a sudden shift in energy to lower frequencies occurs with a significant portion in the range $St = 0.0014 - 0.1$. The energy content in the low frequencies decreases in the separated region but increases near the reattachment location. Downstream of the interaction the energy content appears to be primarily in the high frequency range. Figure 20b shows the spectra for the incoming boundary layer and the peak low frequency location, $x/\delta = -3.75$. The spectra are un-binned. The high frequency content in both locations shows similar behavior whereas the signal taken at $x/\delta = -3.75$ shows significant broadband low frequency content below $St = 0.1$. The low frequency spectra and the time history in figure 19 are consistent with the irregular, aperiodic, broadband behavior observed by Priebe & Martin.[14]

To address the question of how the LFU is modified near the aerodynamic fence we consider the compensated power spectra of wall pressure fluctuations in the region near the aerodynamic fence as shown in figure 21a. The same conventions are used as in figure 20a except that the spectra are averaged in the spanwise direction from the location of the aerodynamic fence to 0.1δ away (towards the center) from the aerodynamic fence. Similar upstream behavior to the center flow spectra is observed with only high frequency content present. A sudden shift down in frequency occurs at the beginning of the aerodynamic fence. The peak low frequency content occurs at $x/\delta = -4.25$, slightly upstream of that observed in the center flow spectra. A large spike in energy is present just above $St = 0.01$, but significant energy is present from $St = 0.01 - 0.1$. There is also significant energy in the low frequency range around $x/\delta = -2$. Downstream of this point the low frequency range is increasingly devoid of energy. The main differences in the wall pressure power spectra between that near the aerodynamic fence and the center flow include a sudden shift to lower frequency at the beginning of the aerodynamic fence, a larger peak value in the low frequency range, and a secondary streamwise location with significant energy in the lower frequencies.

The presence of the aerodynamic fence clearly has a significant impact on the nature and location of low frequency unsteadiness. By taking the integral of the wall pressure power spectra for frequencies below $St = 0.02$, we can observe where in the flow the low frequency dynamics are important. Figures 22a and 22b show the integral of the normalized and un-normalized power spectra below $St = 0.02$. This provides two perspectives on the LFU distribution. The normalized, or relative, energy tells us how much of the energy is

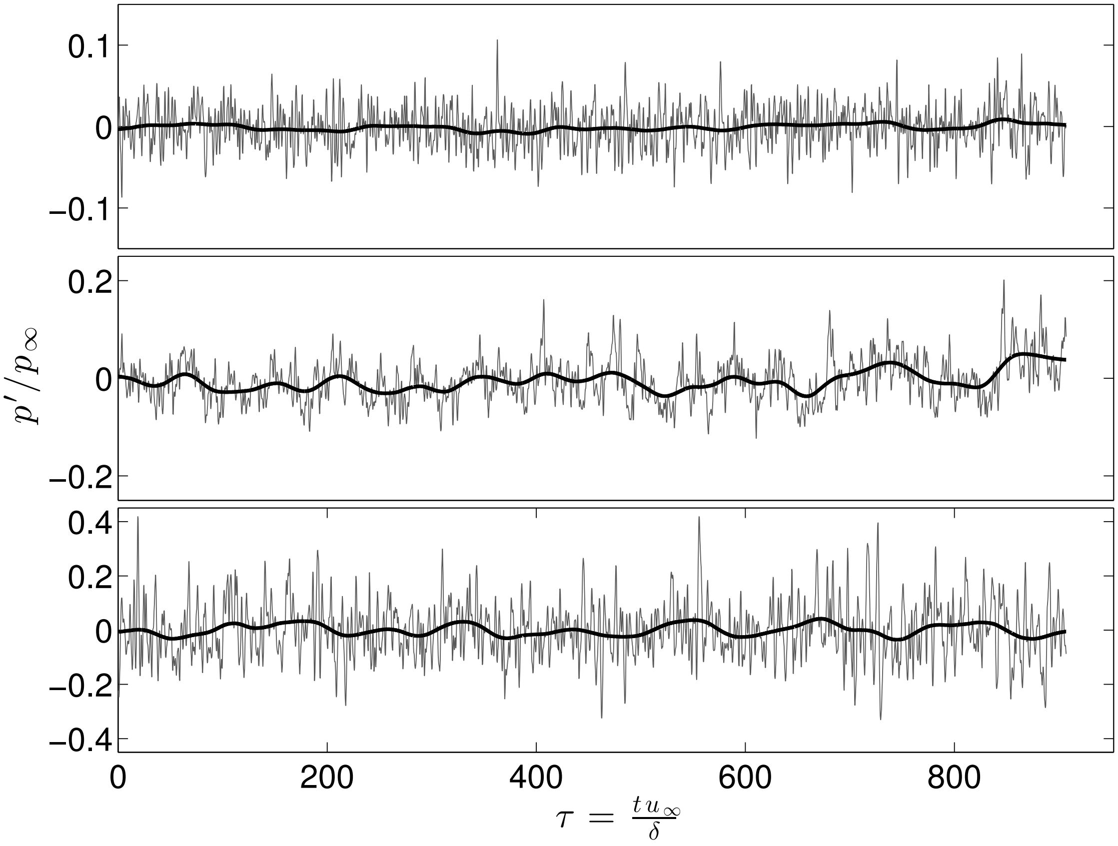

Figure 19: Time history of wall pressure at three streamwise stations, from top to bottom, inflow $x/\delta = -9$, separation $x/\delta = -3.2$, and reattachment $x/\delta = 1.5$. The unfiltered signal is shown in grey while a low pass filtered signal is shown in black to highlight the low frequeny motion. The low pass filtered signal is filtered using a pseudogaussian filter of width $St = 0.02$.

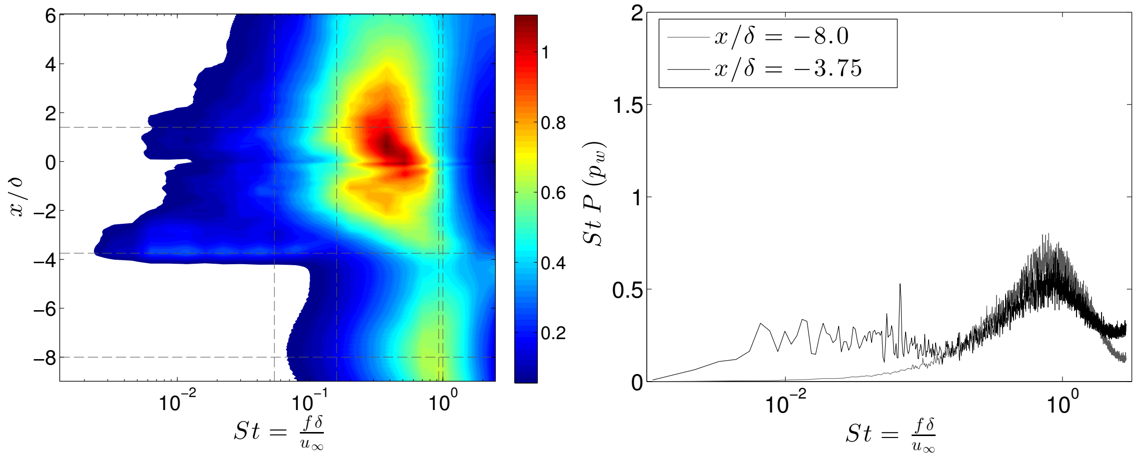

(a) Power Spectra Contours

(b) Power Spectra Signals

Figure 20: Contours of compensated power spectral density of wall pressure fluctuations, $St\ P(p_w)$. The spectra on the left has been binned into 25 logarithmically spaced St bins. The spectra is normalized such that the integral of the energy at each streamwise location is equal to one. The streamwise locations of $x/\delta = -8.0$, -3.75, & 5.0 have been highlighted with horizontal grey dashed lines. Several frequencies associated with the system have been highlighted with vertical grey dashed lines. These frequencies are, from right to left, the boundary layer frequency $St_{BL} = 1$, the convective frequency St_{conv}, the Lagrangian decorrelation frequency St_{LDT}, and the eddy turnover frequency St_{ET}. The spectra are taken at all locations between $z/\delta = -8$ to $z/\delta = 8$ and averaged in the spanwise direction. Un-binned spectra from the upstream boundary layer and separation location are also shown (RIGHT).

contained in the lower frequencies relative to the total energy at a particular location. The un-normalized, or absolute, energy tells us how much energy is contained in the lower frequencies compared with other locations. In both cases, no energy is contained in the lower frequencies upstream of the interaction. A large amount of relative energy is contained in the low-frequencies along the separation line, which moves upstream as it approaches the aerodynamic fence. It's peak value is achieved at the separation point on the aerodynamic fence surface. A secondary peak is present about 2δ upstream of the corner on the aerodynamic fence surface. Although relative energy is contained in the lower frequencies throughout the interation region, it begins to diminish in the recovery region. The absolute energy distribution is somewhat different, with significantly less energy contained in the lower frequencies near the separation point comapred with other parts of the flow. The peak absolute low frequency energy occurs at the reattachment location on the aerodynamic fence surface. Another peak occurs 2δ upstream of the corner on the aerodynamic fence surface, in the same location that was observed in the relative energy.

Figures 23a and 23b show the same quantities as figures 22a and 22b on the surface of the aerodynamic fence. The peak observed in figure 22a at the separation location can be observed to continue along the surface of the aerodynamic fence following the location of the shock. Similarly the peak observed 2δ upstream of the corner, extends along the surface of the aerodynamic fence in the same position as the primary vortex observed in figure 9. From figures 22a through 23b we can conclude that of the energy contained due to motion of the shock, a large fraction of it is contained in the lower frequencies, while the vortex on the aerodynamic fence surface, eminating from the interaction, contains significantly more energy in the lower frequencies, partially due to the overall higher energy content contained within that structure. Ultimately, low frequencies dynamics will impact the pressure loads on aerodynamic fences due to both the shock and coherent vortices extending from the interaction. The effects of these unsteady pressure loads will be critical in the design of efficient flow control structures such as aerodynamic fences.

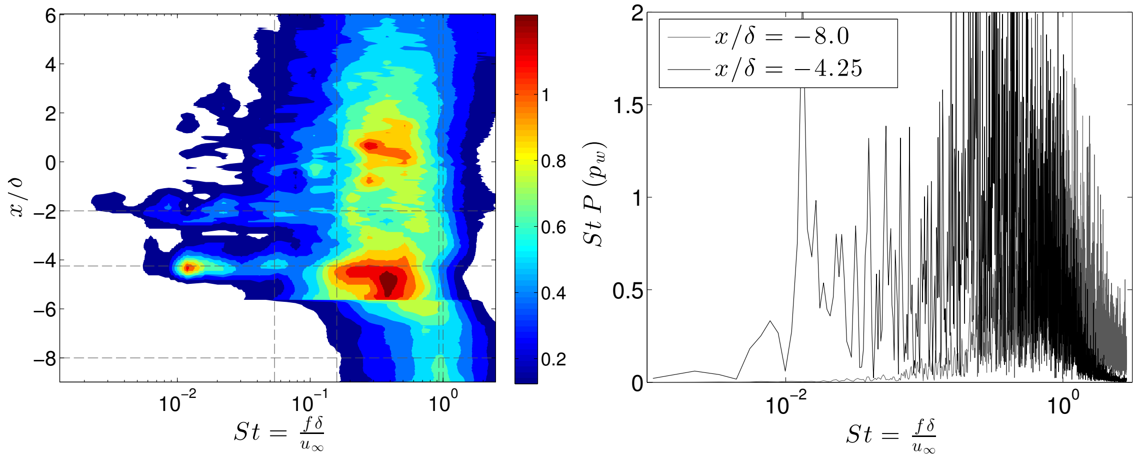

(a) Power Spectra Contours

(b) Power Spectra Signals

Figure 21: Contours of compensated power spectral density of wall pressure fluctuations, $St\,P(p_w)$ taken in near the aerodynamic fence. The spectra on the left has been binned into 25 logarithmically spaced St bins. The spectra is normalized such that the integral of the energy at each streamwise location is equal to one. The streamwise locations of $x/\delta = -8.0$, -4.25, & 5.0 have been highlighted with horizontal grey dashed lines. Several frequencies associated with the system have been highlighted with vertical grey dashed lines. These frequencies are, from right to left, the boundary layer frequency $St_{BL} = 1$, the convective timescale St_{conv}, the Lagrangian decorrelation frequency St_{LDT}, and the eddy turnover frequency St_{ET}. The spectra are taken at all locations between $z/\delta = -11.42$ (aerodynamic fence location) to $z/\delta = -11.32$ and averaged in the spanwise direction. Un-binned spectra from the upstream boundary layer and the location of peak low-frequency content ($x/\delta = -4.25$) are also shown (RIGHT).

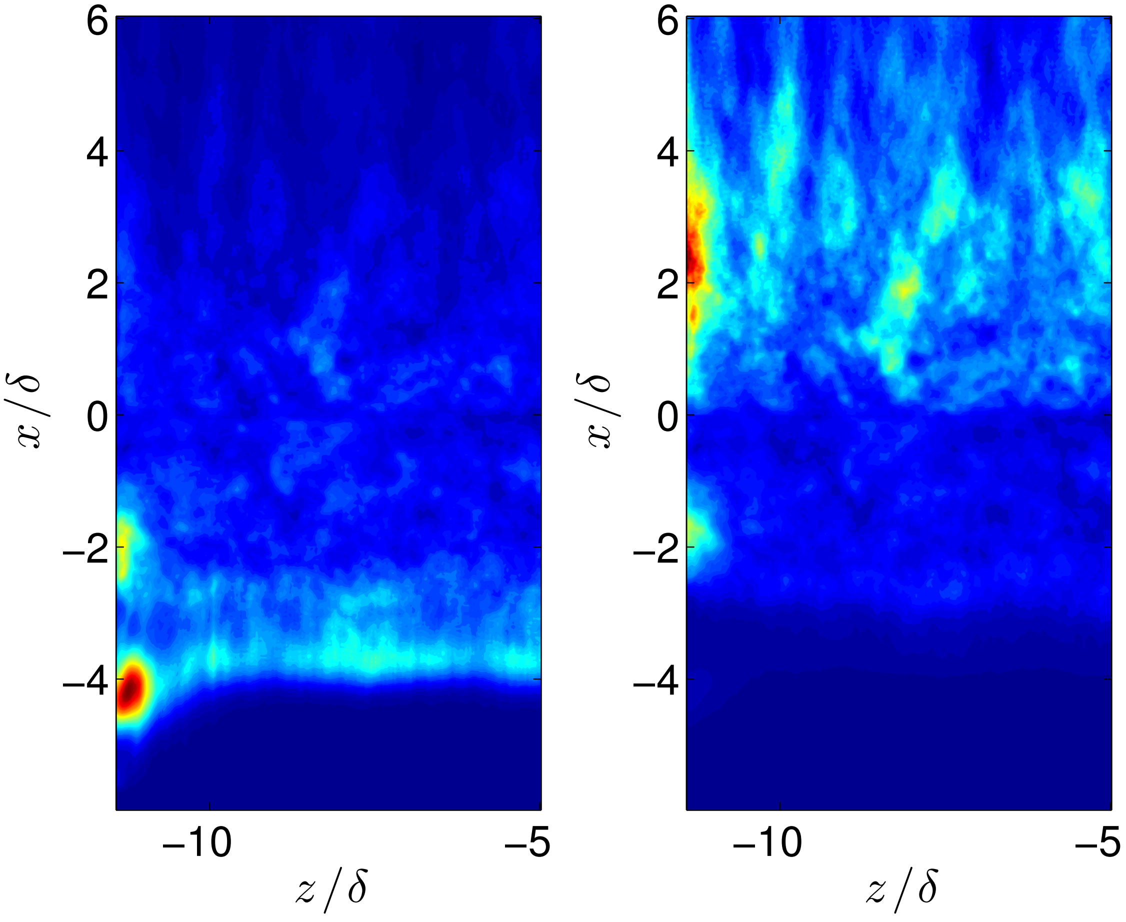

(a) Relative

(b) Absolute

Figure 22: Contours of wall pressure low frequency energy content, defined as the integral of normalized (LEFT) or un-normalized (RIGHT) power spectral density of wall pressure fluctuations below $St = 0.02$. The normalization used is the integral of the power spectra.

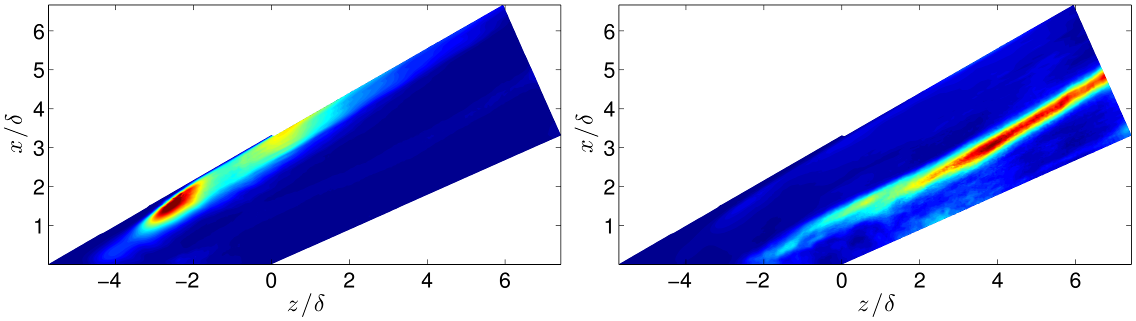

(a) Relative

(b) Absolute

Figure 23: Contours of wall pressure low frequency energy content, defined as the integral of normalized (LEFT) and un-normalized (RIGHT) power spectral density of wall pressure fluctuations below $St = 0.02$. The normaliztion used is the integral of the power spectra.

V. Conclusion

LES has been used to investigate the flow of a $M_\infty = 2.9$ and Momentum Thickness Reynolds number $Re_\theta = 2400$ turbulent boundary layer flowing over a 24° compression ramp with flow confining aerodynamic fences. The solution was validated against centerline data from the experiments of Ringuette *et al.*[30] and Bookey[31] at matching conditions and geometry with excellent agreement. The solution was compared with that from a span periodic calculation to describe the effects of the aerodynamic fences as well as the significantly larger spanwise domain size. It was observed that the span periodic case produced a slightly overpredicted interaction size, resulting in a separation length which was 8% larger than that of the 3D case. The spanwise size of the computational domain is roughly one order of magnitude larger than previous high fidelity, wall resolved studies of STBLI, allowing for the entire experimental configuration to be modeled and eliminating the spanwise periodic, spanwise homogeneous, and narrow span assumptions traditionally used. The flow maintains a nominally two-dimensional configuration roughly 1.5δ away from the aerodynamic fences, and is distorted away from this configuration close to the aerodynamic fences. The primary features observed in the flow near the aerodynamic fences are a secondary shock from the leading edge of the aerodynamic fence which joins the primary separation shock bending it upward and a strong recirculation zone which is initiallly oriented normal to the flat plate, but is bent downstream forming a strong coherent vortex which runs parallel to the ramp surface.

In the center region which is usually assumed to be spanwise homogeneous, large inhomogeneities were observed in skin friction coefficient, streamlines, all three components of the velocity vector, streamwise vorticity, and reattachment location. The critical Görtler number value is exceeded in much of the interaction indicating the likelyhood of these inhomogeneities being caused by Görtler-like vortices. The pattern observed in streamwise vorticity also suggests a Görtler type mechanism as the cause of the inhomogeneities. The large variation observed in skin friction coefficient in the spanwise direction brings into question the utility of using experimental measurements taken at a single spanwise location. We suggest that future experimental investigations collect data at several spanwise locations to better quantify these spanwise variations. Experimental data at multiple locations will go a long way in fascilitating future numerical validation efforts.

In the undisturbed center flow region, low frequency unsteadiness of wall pressure was observed to be present, most prominatly at the separation point and reattachment point. In the region near the shock along the aerodynamic fence, a large fraction of the energy is contained in the low frequency reange. The largest amount of energy from low frequency fluctuations was observed in the primary vortex along the aerodynamic fence. Capturing these low frequency pressure loads may be critical in the efficient design of aerodynamic fences for flight vehicle applications.

Acknowledgments

We would like to thank Dr. I. Bermejo-Moreno and Dr. J. Larsson for their help with $CharLES^x$ as well as Dr. A. Smits of Princeton University and Dr. M. Ringuette of The University of Buffalo for their help in precicely defining the geometry. The first author would like to acknowledge Z. Vane of Stanford University and Dr. B. Morgan of Lawrence Livermore National Laboratory for their many helpful interactions and collaborations.

This work was performed under the auspices of the U.S. Department of Energy by Lawrence Livermore National Laboratory under Contract DE_AC52-07NA27344. Lawrence Livermore National Security, LLC.

References

[1] Dolling, D. S., "Fifty Years of Shock-Wave/Boundary Layer Interaction Research: What Next?" *AIAA Journal*, Vol. 39, No. 8, 2001, pp. 1517–1531.

[2] Wu, M. and Martin, M. P., "Direct Numerical Simulation of Supersonic Turbulent Boundary Layer over a Compression Ramp," *AIAA Journal*, Vol. 45, No. 2, 2007, pp. 879–889.

[3] Settles, G. S., Fitzpatrick, T., and Bogdonoff, S. M., "Detailed Study of Attached and Separated Compression Corner Flowfields in High Reynolds Number Supersonic Flow," *AIAA Journal*, Vol. 17, No. 1, 1979, pp. 579–585.

[4] Zheltovodov, A. A., "Advances and Problems in Modeling of Shockwave Turbulent Boundary Layer Interactions," *Proceedings of the International Conference on the Methods of Aerophysical Research*, Institute of Theoretical and Applied Mechanics, Novosibirsk, Russia, 2004.

[5] Trilling, L., "Oscillating shock-boundary layer interaction," *Journal of the Aerospace Sciences*, Vol. 25, 1958, pp. 301–304.

[6] Andreopoulos, J. and Muck, K. C., "Some New Aspects of The Shock-Wave/Boundary-Layer Interaction in Compression-Ramp Flows," *Journal of Fluid Mechanics*, Vol. 180, 1987, pp. 405–428.

[7] Thomas, F. O., Putnam, C. M., and Chu, H. C., "On the mechanism of unsteady shock oscillation in the shock wave/turbulent boundary layer interactions," *Experiments in Fluids*, Vol. 18, 1994, pp. 69–81.

[8] Ganapathisubramani, B., Clemens, N. T., and Dolling, D. S., "Large-scale motions in a supersonic turbulent boundary layer," *Jounal of Fluid Mechanics*, Vol. 556, 2006, pp. 271–282.

[9] Ganapathisubramni, B., Clemens, N. T., and Dolling, D. S., "Effects of upstream boundary layer on the unsteadiness of shock-induced separation," *Journal of Fluid Mechanics*, Vol. 585, 2007, pp. 369–394.

[10] Dupont, P., Haddad, C., and Debieve, J. F., "Space and time organization in a shock-induced separated boundary layer," *Journal of Fluid Mechanics*, Vol. 559, 2006, pp. 255–277.

[11] Dussauge, J. P., Dupont, P., and Debieve, J. F., "Unsteadiness in shock wave boundary layer interaction with separation," *Aerospace Science and Technology*, Vol. 10, No. 2, 2006, pp. 85–91.

[12] Piponniau, S., Dussauge, J. P., and Debieve, J. F., "A simple model for low-frequency unsteadiness in shock-induced separation," *Journal of Fluid Mechanics*, Vol. 629, 2009.

[13] Wu, M. and Martin, M. P., "Analysis of shock motion in shockwave and turbulent boundary layer interaction using direct numerical simulation data," *Journal of Fluid Mechanics*, Vol. 594, 2008, pp. 71–83.

[14] Priebe, S. and Martin, M. P., "Low-frequency unsteadiness in shock wave-turbulent boundary layer interaction," *Journal of Fluid Mechanics*, Vol. 699, 2012, pp. 1–49.

[15] Morgan, B. E., Duraisamy, K., Nguyen, N., Kawai, S., and Lele, S. K., "Flow physics and RANS modelling of oblique shock/turbulent boundary layer interaction," *Jounal of Fluid Mechanics*, Vol. 729, 2013, pp. 231–284.

[16] Morgan, B. E., *Large-Eddy Simulation Of Shock/Turbulence Interactions In Hypersonic Vehicle Isolator Systems*, Ph.D. thesis, Stanford University, 2012.

[17] Clemens, N. T. and Narayanaswamy, V., "Low-Frequency Unsteadiness of Shock Wave/Turbulent Boundary Layer Interactions," *Annual Review of Fluid Mechanics*, September 2013, pp. 14:46.

[18] Dawson, D. M., Kawai, S., and Lele, S. K., "Large-Eddy Simulation of a Mach 2.9 Turbulent Boundary Layer over a 24° Compression Ramp," *41st AIAA Fluid Dynamics Conference and Exhibit*, 2011.

[19] Dawson, D. M., Bodart, J., and Lele, S. K., "Assessment of Wall-Modeled Large Eddy Simulation for Supersonic Compression Ramp Flows," *AIAA/ASME/SAE/ASEE Joint Propulsion Conference*, 2013.

[20] Edwards, J. R., Choi, J.-I., and Boles, J. A., "Large-Eddy/Reynolds-Averaged Navier-Stokes Simulation of a Mach 5 Compression-Corner Interaction," *AIAA Journal*, Vol. 46, No. 4, April 2008.

[21] Grilli, M., Hickel, S., and Adams, N. A., "Large-eddy simulation of a supersonic turbulent boundary layer over a compression-expansion ramp," *International Journal of Heat and Fluid Flow*, 2013, pp. 79–93.

[22] Grilli, M., Schmid, P. J., Hickel, S., and Adams, N. A., "Analysis of unsteady behaviour in shockwave turbulent boundary layer interaction," *Jounal of Fluid Mechanics*, Vol. 700, 2012, pp. 16–28.

[23] Hadjadj, A., "Large-Eddy Simulation of Shock/Boundary-Layer Interaction," *AIAA Journal*, Vol. 50, No. 12, December 2012.

[24] Hadjadj, A., Larsson, J., Morgan, B. E., Nichols, J. W., and Lele, S. K., "Large-eddy simulation of shock/boundary-layer interaction," *Proceddings of the Summer Program*, Center for Turbulence Research, 2010.

[25] Loginov, M. S., Adams, N. A., and Zheltovodov, A. A., "Large-eddy simulation of shock-wave/turbulent-boundary-layer interaction," *Jounal of Fluid Mechanics*, Vol. 565, 2006, pp. 135–169.

[26] Na, Y. and Moin, P., "Direct numerical simulation of a separated turbulent boundary layer," *Jounal of Fluid Mechanics*, Vol. 374, 1998, pp. 379–405.

[27] Pirozzoli, S. and Grasso, F., "Direct numerical simulation of impinging shock wave/turbulent boundary layer interaction at M=2.25," *Physics of Fluids*, 2006.

[28] Touber, E. and Sandham, N., "Large-eddy simulation of low-frequency unsteadiness in a turbulent shock-induced separation bubble," *Theoretical and Computational Fluid Dynamics*, Vol. 23, 2009, pp. 79–107.

[29] Touber, E. and Sandham, N. D., "Low-order stochastic modelling of low-frequency motions in reflected shock-wave/boundary-layer interactions," *Jounal of Fluid Mechanics*, Vol. 671, 2011, pp. 417–465.

[30] Ringuette, M. J., Bookey, P., Wyckham, C., and Smits, A. J., "Experimental Study of a Mach 3 Compression Ramp Interaction at $Re_\theta = 2400$," *AIAA Journal*, Vol. 47, No. 2, 2009, pp. 373–385.

[31] Bookey, P., *An experimental study of shock/turbulent boundary layer interactions at DNS accessible Reynolds numbers*, Master's thesis, Princeton University, 2005.

[32] Ringuette, M. J., Wu, M., and Martin, M. P., "Low Reynolds Number Effects in a Mach 3 Shock/Turbulent-Boundary-Layer Interaction," *AIAA Journal*, Vol. 46, No. 7, July 2008.

[33] Bermejo-Moreno, I., Larsson, J., Campo, L., Bodart, J., Vicquelin, R., Helmer, D., and Eaton, J., "Wall-modeled large eddy simulation of shock/turbulent boundary-layer interaction in a duct," *Center for Turbulence Research Annual Research Briefs*, 2011, pp. 49–62.

[34] Bermejo-Moreno, I., Larsson, J., Campo, L., Bodart, J., Emory, M., Palacios, F., Helmer, D., Iaccarino, G., and Eaton, J., "Multi-fidelity numerical simulations of shock/turbulent-boundary-layer interaction in a duct with uncertainty quantification," *Center for Turbulence Research Annual Research Briefs*, 2012.

[35] Helmer, D. B., *Measurements of a Three-Dimensional Shock-Boundary Layer Interaction*, Ph.D. thesis, Stanford University, 2011.

[36] Helmer, D. B., Campo, L. M., and Eaton, J. K., "Three-dimensional features of a Mach 2.1 shock/boundary layer interaction," *Experiments in Fluids*, Vol. 53, 2012, pp. 1347–1368.

[37] Khalighi, Y., Nichols, J. W., Lele, S. K., Ham, F., and Moin, P., "Unstructured Large Eddy Simulation for Prediction of Noise Issued from Turbulent Jets in Various Configurations," *Proceedings of the 17th AIAA/CEAS Aeroacoustics Conference*, AIAA, 2011.

[38] Vreman, A., "An eddy-viscosity subgrid-scale model for turbulent shear flow: Algebraic theory and applications," *Physics of Fluids*, Vol. 16, No. 10, 2004, pp. 3670–3681.

[39] You, D. and Moin, P., "A dynamic global-coefficient subgrid-scale eddy-viscosity model for large-eddy simulation in complex geometries," *Physics of Fluids*, Vol. 19, 2007, pp. 065110.

[40] Xie, Z.-T. and Castro, I. P., "Efficient generation of inflow conditions for large eddy simulation of street-scale flows," *Flow, Turbulence, and Combustion*, Vol. 81, 2008, pp. 449–470.

[41] Klein, M., Sadiki, A., and Janicka, J., "A digital filter based generation of inflow data for spatially developing direct numerical or large eddy simulations," *Journal of Computational Physics*, Vol. 186, 2003, pp. 652–665.

[42] Smits, A. J. and Ringuette, M. J., Private Communication, August 2014.

[43] Settles, G. S., *An Experimental Study of Compressible Turbulent Boundary Layer Separation at High Reynolds Numbers*, Princeton University, 1975.

[44] Morgan, B., Larsson, J., Kawai, S., and Lele, S. K., "Improving Low-Frequency Characteristics of Recycling/Rescaling Inflow Turbulence Generation," *AIAA Journal*, Vol. 49, No. 3, 2011, pp. 582–597.

[45] van Driest, E., "Turbulent Boundary Layer in Compressible Fluids," *Journal of the Aeronautical Sciences*, Vol. 18, 1951, pp. 145–160.

[46] Hunt, D. L. and Nixon, D., "A very large eddy simulation of an unsteady shock wave/turbulent boundary layer interaction," *AIAA, Fluid Dynamics Conference, 26th, San Diego, CA*, 1995.

[47] Floryan, J. M., "On The Görtler Instability of Boundary Layers," *Progress in Aerospace Sciences*, Vol. 28, 1991, pp. 235–271.

[48] Tani, I., "Production of longitudinal vortices in the boundary layer along a concave wall," *Journal of Geophysical Research*, 1962.

[49] Theisel, H., *Vector Field Curvature and Applications*, Ph.D. thesis, Universit at Rostock, 1995.

[50] Görtler, H., *On the three-dimensional instability of laminar boundary layers on concave walls*, NACA, 1954.